LETTERS
https://doi.org/10.1038/s41591-019-0375-9
nature medicine

Adult hippocampal neurogenesis is abundant in neurologically healthy subjects and drops sharply in patients with Alzheimer's disease

Elena P. Moreno-Jiménez[1,2,3,6], Miguel Flor-García[1,2,3,6], Julia Terreros-Roncal[1,2,3,6], Alberto Rábano[4], Fabio Cafini[5], Noemí Pallas-Bazarra[1,3], Jesús Ávila[1,3] and María Llorens-Martín[1,2,3*]

The hippocampus is one of the most affected areas in Alzheimer's disease (AD)[1]. Moreover, this structure hosts one of the most unique phenomena of the adult mammalian brain, namely, the addition of new neurons throughout life[2]. This process, called adult hippocampal neurogenesis (AHN), confers an unparalleled degree of plasticity to the entire hippocampal circuitry[3,4]. Nonetheless, direct evidence of AHN in humans has remained elusive. Thus, determining whether new neurons are continuously incorporated into the human dentate gyrus (DG) during physiological and pathological aging is a crucial question with outstanding therapeutic potential. By combining human brain samples obtained under tightly controlled conditions and state-of-the-art tissue processing methods, we identified thousands of immature neurons in the DG of neurologically healthy human subjects up to the ninth decade of life. These neurons exhibited variable degrees of maturation along differentiation stages of AHN. In sharp contrast, the number and maturation of these neurons progressively declined as AD advanced. These results demonstrate the persistence of AHN during both physiological and pathological aging in humans and provide evidence for impaired neurogenesis as a potentially relevant mechanism underlying memory deficits in AD that might be amenable to novel therapeutic strategies.

The occurrence of AHN in humans was first shown by Eriksson et al.[5]. Their findings have been supported[6–8] and questioned[9,10] by a number of subsequent studies. However, the limited availability of adequately preserved human brain tissue samples, together with the heterogeneity of tissue processing methodologies, is considered to have contributed to a lack of consensus in this regard[11]. To shed light on the potential occurrence of AHN during physiological human aging, we sought to determine whether the adult human DG harbors a population of immature neurons throughout life (Fig. 1). To this end, we first established the most suitable conditions in which to study AHN in humans. We used brain samples obtained under tightly controlled conditions and state-of-the-art tissue processing methodologies (Methods and Extended Data Figs. 1–6). These conditions involved careful evaluation of medical records, exclusion of subjects showing any neurological disease or cognitive disability, and confirmation of Braak stage 0 by neuropathological examination (Methods). We also monitored the post-mortem delay (PMD; the time lapse between exitus and tissue immersion in fixative), optimized fixation time and conditions, and avoided freezing, paraffin inclusion, or any type of mechanical alteration of the tissue. Under these methodological constraints, we identified thousands of doublecortin-expressing (DCX$^+$) neurons in the DG for a cohort of 13 neurologically healthy subjects between 43 and 87 years of age (Fig. 1d,h,j and Extended Data Figs. 1–4 and 6c). These findings were further confirmed using four anti-DCX antibodies raised against different parts of the protein (Extended Data Fig. 4). We noted that the DCX signal was absent in non-neurogenic brain regions such as the entorhinal cortex (EC) (Fig. 1b,f and Extended Data Fig. 6a) and in the CA1 (Fig. 1c,g and Extended Data Fig. 6b) and CA3 (Fig. 1e,i and Extended Data Fig. 6d) hippocampal subfields.

AHN is a tightly regulated process that encompasses a well-characterized sequence of maturation stages in rodents[12]. After exiting the cell cycle, immature neuroblasts go through a series of differentiation phases before becoming fully mature. In rodents, DCX expression occurs during most of the differentiation stages of AHN, and the population of DCX$^+$ cells in consequence exhibits varying degrees of maturation[11–13]. Therefore, we addressed whether cell subpopulations at distinct stages of maturity could also be distinguished among DCX$^+$ cells in the human DG (Fig. 2). To this end, we first analyzed the expression of cell markers characteristic of the different maturation stages of AHN[11,12] in human DCX$^+$ cells (Fig. 2a–i). Notably, 91% of DCX$^+$ cells also expressed prospero homeobox 1 (Prox1) (Fig. 2c,i), thereby suggesting that most DCX$^+$ cells had already acquired a dentate granule cell (DGC) fate[14] and validating DCX as a reliable marker of immature DGCs in humans. Accordingly, a subset of DCX$^+$ cells were positive for markers transiently expressed by immature neurons, such as polysialic acid–neural cell adhesion molecule (PSA-NCAM) (Fig. 2d,i) and calretinin (CR) (Fig. 2e,i). Approximately 40–60% of DCX$^+$ cells expressed markers of neuronal identity such as neuronal nuclei (NeuN) (Fig. 2f,i), βIII-tubulin (Fig. 2g,i), and tau (Fig. 2i). Finally, ~40% of DCX$^+$ cells expressed markers of more differentiated neurons, such as calbindin (CB) (Fig. 2h,i).

During AHN in rodents, differential expression of two calcium-binding proteins, CR and CB, defines two postmitotic maturation stages of DGCs[12,15]. CR is transiently expressed by immature neurons during early differentiation phases, whereas CB expression is characteristic of more differentiated DGCs[15]. Expression of these

[1]Department of Molecular Neuropathology, Centro de Biología Molecular 'Severo Ochoa', CBMSO, CSIC-UAM, Madrid, Spain. [2]Department of Molecular Biology, Faculty of Sciences, Universidad Autónoma de Madrid, Madrid, Spain. [3]Center for Networked Biomedical Research on Neurodegenerative Diseases (CIBERNED), Madrid, Spain. [4]Neuropathology Department, CIEN Foundation, Madrid, Spain. [5]Universidad Europea de Madrid, Faculty of Biomedical and Health Sciences, Madrid, Spain. [6]These authors contributed equally: E. P. Moreno-Jiménez, M. Flor-García, J. Terreros-Roncal.
*e-mail: m.llorens@csic.es

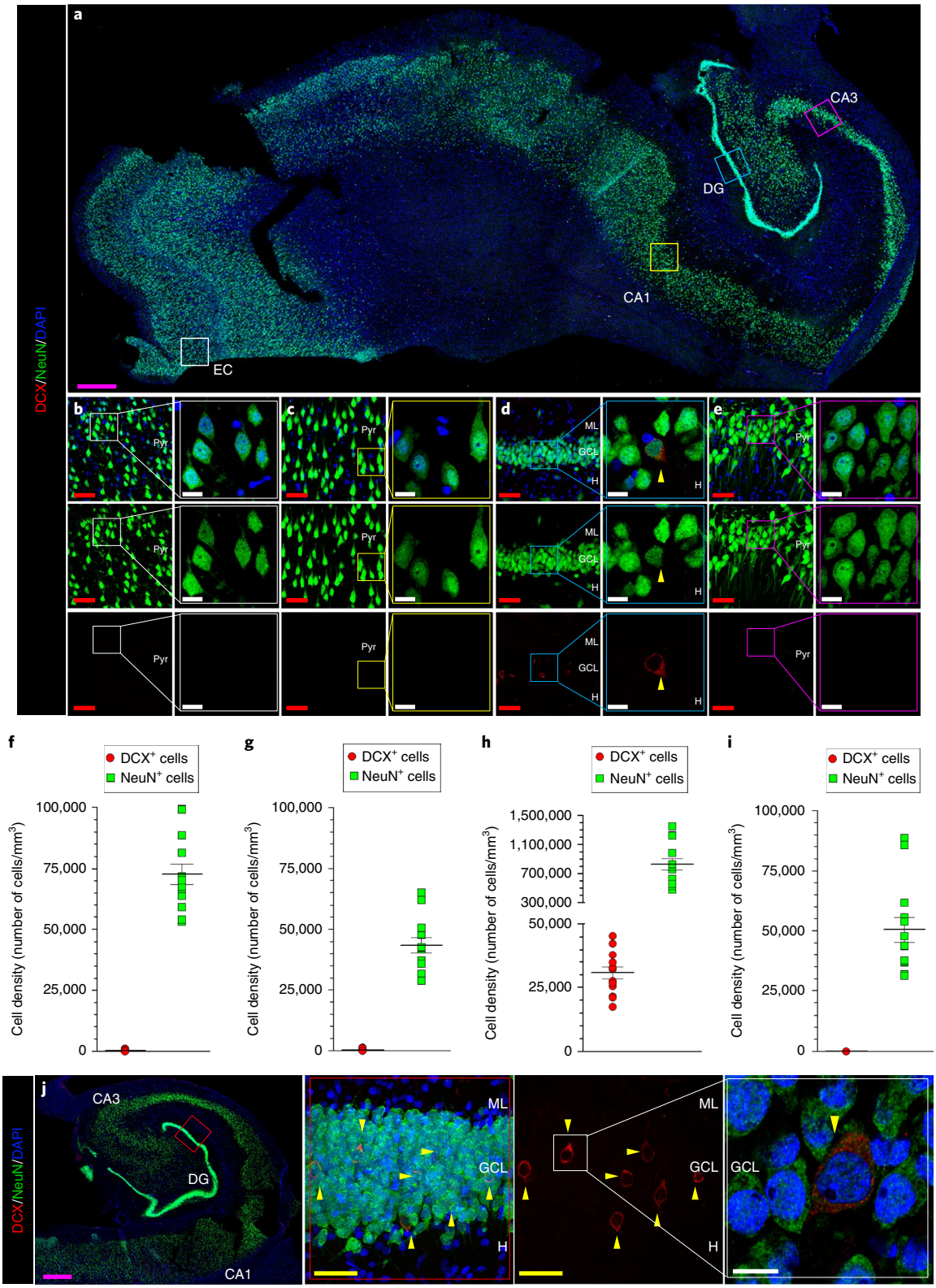

Fig. 1 | Adult hippocampal neurogenesis is a robust phenomenon in the dentate gyrus of neurologically healthy adult human subjects. a–e, Representative tile scan acquisition image comprising the whole human hippocampus and the EC (level 38 in the Human Brain Atlas[26]) (**a**) and magnification of the EC (**b**), CA1 (**c**), DG (**d**), and CA3 (**e**) hippocampal subfields. These images show absence of DCX staining in non-neurogenic regions (**b**,**c**,**e**) and abundant presence of DCX+ cells in the DG (**d**). **f–i**, Density of cells expressing DCX and NeuN in the EC (**f**) and in the CA1 (**g**), DG (**h**), and CA3 (**i**) hippocampal subfields for a cohort of 13 neurologically healthy human subjects between 43 and 87 years of age. In **f–i**, graphs represent mean values ± s.e.m. **j**, Tile scan acquisition image comprising the whole human hippocampus (left), together with representative images of the DG showing the abundant presence of DCX+ immature neurons (center) and a high-power-magnification image showing the morphology of one of these cells (right). In **a–j**, $n = 13$ control subjects. For each subject, 10–20 stacks of images per region were obtained to determine cell densities. Pyr, pyramidal layer; ML, molecular layer; GCL, granule cell layer; H, hilus. Magenta scale bars, 200 μm; red and yellow scale bars, 50 μm; white scale bars, 10 μm. Yellow triangles indicate DCX+ cells.

two cell markers also correlates with different morphological features[16]. Accordingly, remarkable morphological heterogeneity was observed among DCX+ cells in the human DG (Fig. 2k–m). Thus, we questioned whether this morphological heterogeneity also reflects distinct maturation stages. To examine this, we analyzed the morphological features of double-labeled (DCX+CR+ and DCX+CB+) cells. Notably, DCX+CR+ cells were predominantly located at the hilar border of the granule cell layer (GCL) (Fig. 2k,o), referred to as the subgranular zone (SGZ). They had smaller soma (Fig. 2k,n), an elongated morphology characteristic of immature DGCs (Fig. 2k), and ~2 primary neurites per cell (Fig. 2k,p), which were mainly oriented parallel to the SGZ (Fig. 2k,q). These observations support the notion that DCX+CR+ cells have an immature phenotype[16]. In contrast, most DCX+CB+ cells occupied deeper positions within the GCL (Fig. 2l,o). They also exhibited larger cell soma (Fig. 2l,n), an oval-to-round morphology (Fig. 2l), and one primary apical neurite (Fig. 2l,p), which was mainly oriented perpendicular to the SGZ, toward the molecular layer (ML) (Fig. 2l,q). These features correlate with a more mature phenotype for this cell population[16].

Altogether, these data strongly support the notion that subpopulations of DCX+ cells have a variable degree of maturation in the human DG. Although birthdating analyses are required to determine the exact duration of individual maturation stages for human DGCs, completion of the maturation process has been proposed to take several months[17] or years[9] in primates. The relative abundance of DCX+ immature neurons detected, together with expression of cell markers characteristic of both early and late stages of maturation, suggests that these cells also have an extended maturation period during AHN in humans. On the basis of both the percentages of double-labeled cells and their morphological features, here we outline the first model of the differentiation stages of human AHN (Fig. 2j).

Our data support the persistence of AHN in the adult human DG until the ninth decade of life. However, recent studies failed to detect high numbers of DCX+ cells in the human hippocampus[9,10]. Therefore, we examined the extent to which heterogeneity in tissue processing could account for the different results. We found that detection of AHN markers in the human DG is critically dependent on fixation conditions and histological pretreatment of the tissue (Extended Data Figs. 2–5 and 7). Our data demonstrate that the prolonged or uncontrolled fixation conditions to which human samples are typically exposed in brain banks worldwide lead to a sharp reduction in the number of DCX+ cells detected in the adult DG (Extended Data Fig. 2). Nonetheless, implementation of the most suitable tissue processing methodologies unraveled the presence of thousands of DCX+ cells with an unambiguously identifiable neuronal morphology in the adult DG. Given this observation, AHN clearly emerges as a robust phenomenon during physiological aging in humans.

The hippocampus is one of the brain regions most affected in AD[1,18], and DGCs exhibit remarkable morphological alterations in patients with AD[18]. Given the role that immature neurons have in hippocampus-dependent learning[3], as well as the alterations in AHN observed in numerous animal models of the disease[19], we decided to study this process in a cohort of 45 patients with AD between 52 and 97 years of age distributed among the six neuropathological Braak stages of the disease[20] (Fig. 3a–c and Extended Data Figs. 7a,b and 8a–g). Stereological estimation of the number of DCX+ cells revealed a marked and progressive decline in this number as the disease advanced (Fig. 3d–k). We also observed that the number of DCX+ cells decreased moderately as age increased from 40 to 90 years in neurologically healthy control individuals (Extended Data Fig. 1b). These data are in agreement with previous evidence suggesting a modest decline in the rate of AHN during physiological aging in humans[6]. However, the number of DCX+ cells detected in neurologically healthy individuals of any age was consistently higher than that found in patients with AD, regardless of the age of these patients (Fig. 3l). These data strongly support the notion that AD is a condition that differs from physiological aging and suggest that, despite a physiological age-related decline in the population of DCX+ cells, independent neuropathological mechanisms contribute to devastating the population of immature neurons in AD.

Given that newborn neurons that do not adequately complete maturation and synaptic integration programs are promptly eliminated during AHN in rodents[12,21], a reduction in either the addition or the survival of immature neurons might underlie the marked decline in cellular counts observed in patients with AD. Thus, we considered it pertinent to determine whether a blockade occurs in the maturation of DCX+ cells in the DG of patients with AD. To this end, we studied the expression of cell markers related to distinct maturation stages during AHN[8,11,12] in DCX+ cells from these patients (Fig. 4). We detected a reduction in the percentage of DCX+ cells that expressed PSA-NCAM (Fig. 4a,d) starting at Braak stage III. This was followed by a reduction in the expression of Prox1 (Fig. 4f), NeuN (Fig. 4g), βIII-tubulin (Fig. 4h), and CB (Fig. 4b,i) at some of the subsequent stages of the disease. These data provide evidence of substantial impairment of the maturation of DCX+ cells as AD advances. Given the unique electrophysiological properties of immature DGCs in rodents[22,23], the aforementioned alterations could be related to the selective impairment of certain types of hippocampus-dependent learning observed in patients with AD[24].

Notably, alterations in AHN were detected at early stages of the disease, even before the generalized presence of neurofibrillary tangles or senile plaques in the DG (Fig. 3a–c and

Fig. 2 | Differentiation stages of adult hippocampal neurogenesis in the dentate gyrus of neurologically healthy adult human subjects. a–h, Expression patterns of cell markers characteristic of different maturation stages during AHN in the human DG, together with high-power-magnification images showing the expression of these markers in DCX+ cells. **a**, Glial fibrillary acidic protein (GFAP). **b**, Phosphorylated histone 3 (PH3). **c**, Prospero homeobox 1 (Prox1). **d**, Polysialic acid–neural cell adhesion molecule (PSA-NCAM). **e**, Calretinin (CR). **f**, Neuronal nuclei (NeuN). **g**, βIII-tubulin. **h**, Calbindin (CB). **i**, Colocalization of DCX and various cell markers. Data are presented as the percentage of double-labeled DCX+ cells. The graph represents mean values ± s.e.m. In **a–i**, $n = 13$ control subjects. At least 100 cells per subject and cell marker were analyzed. **j**, Maturation model detailing the differentiation stages of AHN in humans. **k–q**, Morphological features of double-labeled DCX+CR+ and DCX+CB+ cells. **k**,**l**, Representative images and high-power magnification of DCX+CR+ (**k**) and DCX+CB+ (**l**) cells. **m**, Soma area of DCX+ cells, suggesting the presence of distinct cell subpopulations. The graph represents the mean value. $n = 910$ cells measured independently. **n**, Soma area of double-labeled cells (two-sided Student's *t*-test; $t_{463} = 13.98$, $P < 0.0001$). Graphs represent mean values. $n = 224$ DCX+CR+ and 243 DCX+CB+ cells measured independently. **o**, Cell location within the GCL (two-sided Student's *t*-test; SGZ: $t_{25} = 14.97$, $P < 0.0001$; GCL: $t_{25} = 14.97$, $P < 0.0001$). $n = 13$ control subjects. **p**, Percentage of cells exhibiting 1, 2, 3, or 4 primary dendrites (two-sided Student's *t*-test; 1 neurite: $t_{25} = 9.297$, $P < 0.0001$; 2 neurites: $t_{25} = 6.906$, $P < 0.0001$; 3 neurites: $t_{25} = 4.71$, $P < 0.0001$). $n = 13$ control subjects. **q**, Percentage of cells exhibiting neurites oriented parallel (horizontal) or perpendicular (vertical) to the SGZ and toward the ML (two-sided Student's *t*-test; horizontal neurites: $t_{25} = 17.72$, $P < 0.0001$; vertical neurites: $t_{25} = 17.72$, $P < 0.0001$). $n = 13$ control subjects. RGL, radial-glia-like. In **a–h** and **k–l**, the blue color shows DAPI staining. Yellow scale bars, 50 μm; orange scale bars, 25 μm; blue scale bars, 10 μm. Magenta triangles indicate DCX+ cells; white triangles indicate the presence of neurites for DCX+ cells. In **i**, 4R-Tau refers to 4-repeat Tau isoform. ***$P < 0.001$.

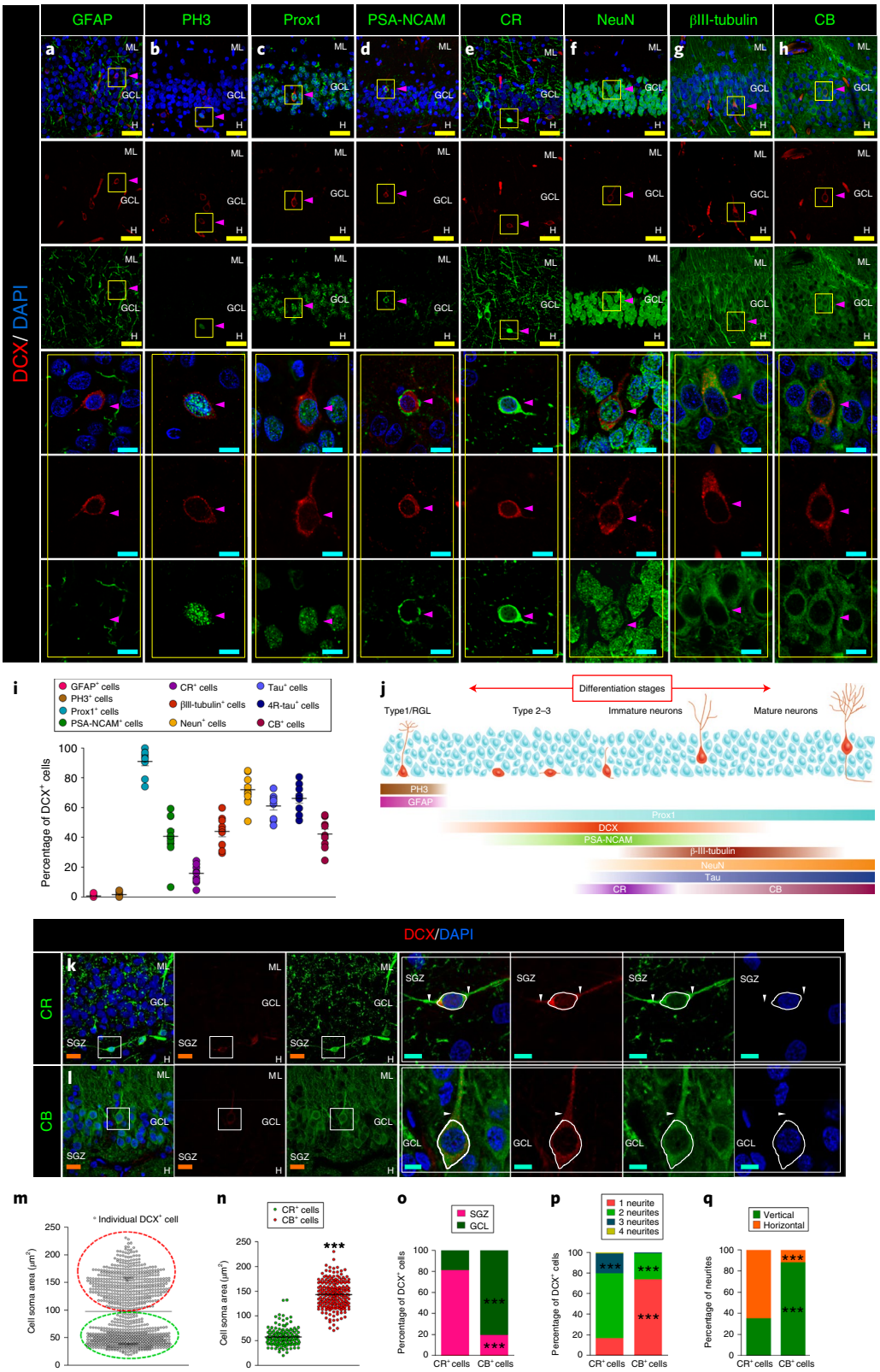

Extended Data Fig. 8). Similarly, various alterations have been proposed to occur during the prodromal stages of the disease, which are believed to start several decades before manifestation of the first clinical symptoms[25]. Therefore, early detection of AHN impairments by noninvasive methods might allow these alterations to be used as relevant biomarkers of the advance of the disease. Moreover, therapeutic strategies aimed at increasing the numbers and functionality of these cells might be relevant to prevent or slow down AD progression.

Our data bring to light the existence of a dynamic population of immature neurons in the human DG throughout physiological and pathological aging until the tenth decade of life. This finding points to unexplored mechanisms of circuit plasticity in the aging human hippocampus. Of note, our results demonstrate a profound,

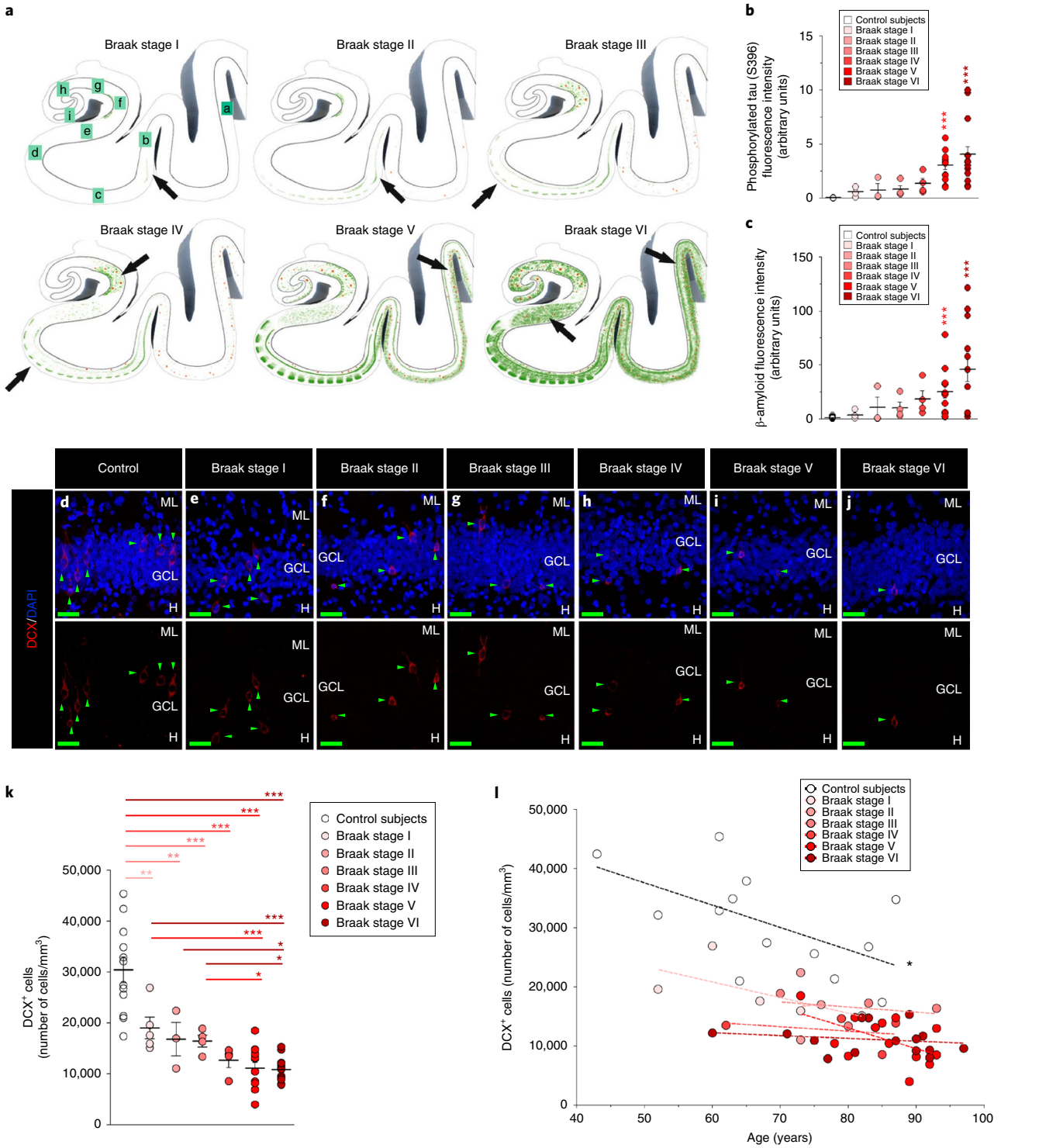

Fig. 3 | Adult hippocampal neurogenesis is impaired in patients with Alzheimer's disease. a, Schematic diagram showing progression of the neuropathological hallmarks of the disease according to the model proposed by Braak and Braak[1,20]. Senile plaques are shown in red, and neurofibrillary tangles are in green. Hippocampal regions are labeled with lowercase letters: temporal cortex (a), transentorhinal cortex (b), entorhinal cortex (c), presubiculum (d), subinculum (e), CA1 (f), CA2 (g), CA3/CA4 (h), and DG (i). In **a**, arrows indicate the brain areas in which neuropathological alterations start to be observed at each Braak stage. **b**, Fluorescence intensity of phosphorylated tau (Ser396) in the DG (one-way ANOVA, $F_{7,58}=8.936$, $P<0.0001$). **c**, Fluorescence intensity of β-amyloid in the DG (one-way ANOVA, $F_{7,58}=4.393$, $P=0.0012$). In **b** and **c**, graphs represent mean values ± s.e.m. $n=13$ control subjects and 45 patients with AD. **d**–**j**, Representative images of DCX staining in the DG of control subjects and patients with AD. In **d**–**j**, the blue color indicates DAPI staining. Top images show merged staining (DCX/DAPI). Bottom images show DCX staining. **k**, Density of DCX$^+$ cells (one-way ANOVA, $F_{7,57}=20.05$, $P<0.0001$). The graph represents mean values ± s.e.m. **l**, Correlation between the density of DCX$^+$ cells and age, in the six Braak stages (two-sided Pearson's correlation, $r=-0.5842$, $P=0.036$). A statistically significant correlation between these parameters was observed only in control subjects. In **d**–**l**, $n=13$ control subjects and 45 patients with AD. Twenty measurements were performed for each subject to determine the density of DCX$^+$ cells. Green scale bars, 50 μm. Green triangles indicate DCX$^+$ cells. *$0.05>P\geq0.01$; **$0.01>P\geq0.001$; ***$P<0.001$. In **b**, **c**, and **k**, asterisks indicate significant differences with respect to control subjects in Tukey post hoc comparisons. In **l**, the black asterisk indicates statistical significance in Pearson's correlation for the group of control subjects.

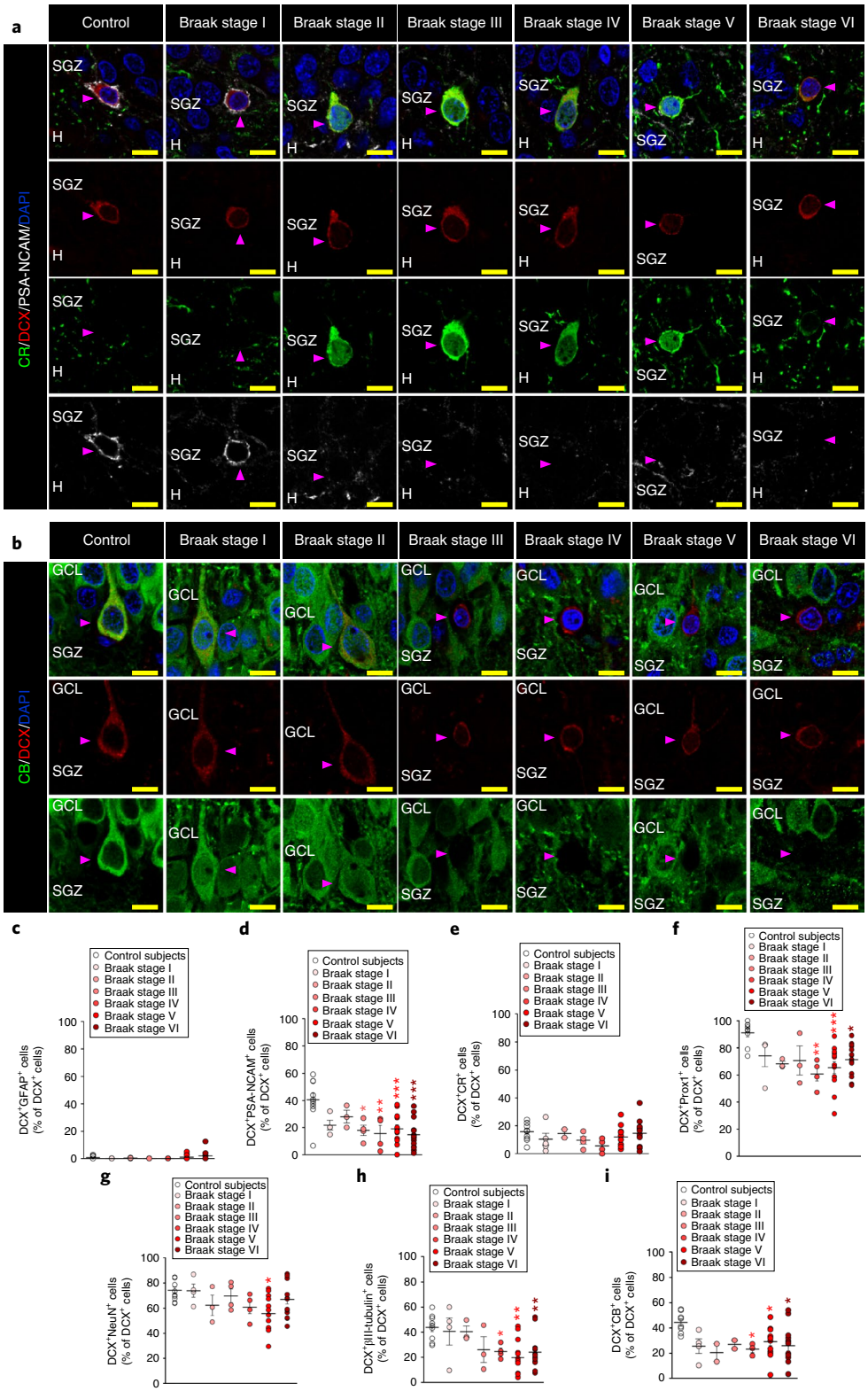

Fig. 4 | Maturation of DCX⁺ cells is impaired in the dentate gyrus of patients with Alzheimer's disease. a,**b**, Representative images showing the expression of markers of immature neurons, such as CR and PSA-NCAM (**a**), and mature neurons, such as CB (**b**), in DCX⁺ cells from control subjects and patients with AD. **c**–**i**, Percentage of DCX⁺ cells expressing GFAP (one-way ANOVA, $F_{7,57}=0.8071$, $P=0.5702$) (**c**), PSA-NCAM (one-way ANOVA, $F_{7,57}=6.03$, $P<0.0001$) (**d**), CR (one-way ANOVA, $F_{7,57}=1.235$, $P=0.3066$) (**e**), Prox1 (one-way ANOVA, $F_{7,57}=4.433$, $P=0.0014$) (**f**), NeuN (one-way ANOVA, $F_{7,57}=2.792$, $P=0.0215$) (**g**), βIII-tubulin (one-way ANOVA, $F_{7,57}=4.219$, $P=0.002$) (**h**), and CB (one-way ANOVA, $F_{7,57}=2.674$, $P=0.0286$) (**i**). In **c**–**i**, graphs represent mean values ± s.e.m. $n=13$ control subjects and 45 patients with AD. Twenty measurements were performed for each subject to determine the density of DCX⁺ cells. In colocalization analyses (**a**–**i**), at least 100 cells per subject were analyzed for each cell marker. Yellow scale bars, 10 μm. Magenta triangles indicate DCX⁺ cells. *$0.05>P\geq0.01$; **$0.01>P\geq0.001$; ***$P<0.001$. Asterisks indicate significant differences with respect to control subjects in Tukey post hoc comparisons.

multifaceted impairment of AHN in patients with AD starting at early stages of the condition. Therefore, restoration of normal levels of AHN in these patients emerges as a potential therapeutic approach to counteract the progression of this as yet incurable disease.

Online content

Any methods, additional references, Nature Research reporting summaries, source data, statements of data availability and associated accession codes are available at https://doi.org/10.1038/s41591-019-0375-9.

Received: 23 October 2018; Accepted: 24 January 2019;
Published online: 25 March 2019

References

1. Braak, H. & Braak, E. Morphology of Alzheimer disease. *Fortschr. Med.* **108**, 621–624 (1990).
2. Altman, J. Autoradiographic investigation of cell proliferation in the brains of rats and cats. *Anat. Rec.* **145**, 573–591 (1963).
3. Sahay, A. et al. Increasing adult hippocampal neurogenesis is sufficient to improve pattern separation. *Nature* **472**, 466–470 (2011).
4. Anacker, C. et al. Hippocampal neurogenesis confers stress resilience by inhibiting the ventral dentate gyrus. *Nature* **559**, 98–102 (2018).
5. Eriksson, P. S. et al. Neurogenesis in the adult human hippocampus. *Nat. Med.* **4**, 1313–1317 (1998).
6. Spalding, K. L. et al. Dynamics of hippocampal neurogenesis in adult humans. *Cell* **153**, 1219–1227 (2013).
7. Boldrini, M. et al. Human hippocampal neurogenesis persists throughout aging. *Cell Stem Cell* **22**, 589–599 (2018).
8. Knoth, R. et al. Murine features of neurogenesis in the human hippocampus across the lifespan from 0 to 100 years. *PLoS ONE* **5**, e8809 (2010).
9. Sorrells, S. F. et al. Human hippocampal neurogenesis drops sharply in children to undetectable levels in adults. *Nature* **555**, 377–381 (2018).
10. Cipriani, S. et al. Hippocampal radial glial subtypes and their neurogenic potential in human fetuses and healthy and Alzheimer's disease adults. *Cereb. Cortex* **28**, 2458–2478 (2018).
11. Kempermann, G. et al. Human adult neurogenesis: evidence and remaining questions. *Cell Stem Cell* **23**, 25–30 (2018).
12. Kempermann, G., Jessberger, S., Steiner, B. & Kronenberg, G. Milestones of neuronal development in the adult hippocampus. *Trends Neurosci.* **27**, 447–452 (2004).
13. Plumpe, T. et al. Variability of doublecortin-associated dendrite maturation in adult hippocampal neurogenesis is independent of the regulation of precursor cell proliferation. *BMC Neurosci.* **7**, 77 (2006).
14. Karalay, O. et al. Prospero-related homeobox 1 gene (*Prox1*) is regulated by canonical Wnt signaling and has a stage-specific role in adult hippocampal neurogenesis. *Proc. Natl Acad. Sci. USA* **108**, 5807–5812 (2011).
15. Brandt, M. D. et al. Transient calretinin expression defines early postmitotic step of neuronal differentiation in adult hippocampal neurogenesis of mice. *Mol. Cell. Neurosci.* **24**, 603–613 (2003).
16. Zhao, C., Teng, E. M., Summers, R. G. Jr, Ming, G. L. & Gage, F. H. Distinct morphological stages of dentate granule neuron maturation in the adult mouse hippocampus. *J. Neurosci.* **26**, 3–11 (2006).
17. Kohler, S. J., Williams, N. I., Stanton, G. B., Cameron, J. L. & Greenough, W. T. Maturation time of new granule cells in the dentate gyrus of adult macaque monkeys exceeds six months. *Proc. Natl Acad. Sci. USA* **108**, 10326–10331 (2011).
18. Llorens-Martin, M. et al. GSK-3β overexpression causes reversible alterations on postsynaptic densities and dendritic morphology of hippocampal granule neurons in vivo. *Mol. Psychiatry* **18**, 451–460 (2013).
19. Lazarov, O., Mattson, M. P., Peterson, D. A., Pimplikar, S. W. & van Praag, H. When neurogenesis encounters aging and disease. *Trends Neurosci.* **33**, 569–579 (2010).
20. Braak, H. & Braak, E. Staging of Alzheimer's disease–related neurofibrillary changes. *Neurobiol. Aging* **16**, 271–278 (1995).
21. Sierra, A. et al. Microglia shape adult hippocampal neurogenesis through apoptosis-coupled phagocytosis. *Cell Stem Cell* **7**, 483–495 (2010).
22. Marin-Burgin, A., Mongiat, L. A., Pardi, M. B. & Schinder, A. F. Unique processing during a period of high excitation/inhibition balance in adult-born neurons. *Science* **335**, 1238–1242 (2012).
23. Bischofberger, J. Young and excitable: new neurons in memory networks. *Nat. Neurosci.* **10**, 273–275 (2007).
24. Wesnes, K. A., Annas, P., Basun, H., Edgar, C. & Blennow, K. Performance on a pattern separation task by Alzheimer's patients shows possible links between disrupted dentate gyrus activity and apolipoprotein E4 in status and cerebrospinal fluid amyloid-β42 levels. *Alzheimers Res. Ther.* **6**, 20 (2014).
25. Heneka, M. T. et al. Neuroinflammation in Alzheimer's disease. *Lancet Neurol.* **14**, 388–405 (2015).
26. Mai, J., Majtanik, M. & Paxinos, G. *Atlas of the Human Brain* (Academic Press, 2008).

Acknowledgements

The authors would like to thank the patients and their families for generously donating brain samples. Moreover, they would like to thank I. Rodal for help with human sample extraction and processing, E. García, R. Cuadros and the confocal microscopy facility of the CBMSO for technical assistance, and P. Moreno for help with illustration design. A number of human samples were generously provided by the Biobanco del Hospital Universitario Reina Sofia (Córdoba, Spain). The authors are grateful to R. Sánchez for providing some of these samples. They would also like to thank J. Gleeson (University of California, San Diego) for providing an anti-DCX antibody. This study was supported by the following: the Spanish Ministry of Economy and Competitiveness (SAF-2017-82185-R and RYC-2015-171899, M.L.-M.; SAF-2014-53040-P, J.Á.); the Alzheimer's Association (2015-NIRG-340709 and AARG-17-528125, M.L.-M.); the Association for Frontotemporal Degeneration (2016 Basic Science Pilot Grant Award, M.L.-M.); the Comunidad de Madrid (PEJD-2017-PRE/BMD-3439, M.L.-M.); and the Center for Networked Biomedical Research on Neurodegenerative Diseases (CIBERNED, Spain, J.Á.). Institutional grants from the Fundación Ramón Areces and the Banco de Santander to CBMSO are also acknowledged. The salary of E.P.M.-J. was supported by a Comunidad de Madrid researcher contract (PEJD-2017-PRE/BMD-3439). The salary of J.T.-R. was supported by a Universidad Autónoma de Madrid doctoral fellowship (FPI-UAM 2017 program).

Author contributions

E.P.M.-J., M.F.-G., J.T.-R., and M.L.-M. designed and conceived the experiments. A.R. provided materials and performed autopsies. M.L.-M. sectioned human samples. E.P.M.-J., M.F.-G., J.T.-R., A.R., F.C., N.P.-B., and M.L.-M. performed the experiments and acquired confocal images. E.P.M.-J., F.C., and M.L.-M. performed cell counts and analyzed the data. M.L.-M. wrote the manuscript. J.Á. and M.L.-M. obtained funding. All authors critically discussed the data and revised the final version of the manuscript.

Competing interests

The authors declare no competing interests.

Additional information

Extended data is available for this paper at https://doi.org/10.1038/s41591-019-0375-9.

Supplementary information is available for this paper at https://doi.org/10.1038/s41591-019-0375-9.

Reprints and permissions information is available at www.nature.com/reprints.

Correspondence and requests for materials should be addressed to M.L.-M.

Methods

Experimental design. The main objective of this work was to confirm the occurrence of AHN in the human DG. To this end, we used human samples obtained under tightly controlled conditions and state-of-the-art methods for tissue processing and preservation (Figs. 1 and 2, and Extended Data Figs. 1–6). We analyzed the presence of DCX-expressing cells in the DG and in non-neurogenic areas (namely, the EC, and the CA1 and the CA3 hippocampal subfields) (Fig. 1). Moreover, we characterized the maturation dynamics of these cells in the DG (Fig. 2). Next, we analyzed the number and maturation of immature neurons in patients with AD (Figs. 3 and 4 and Extended Data Figs. 7 and 8).

Study of the differentiation stages of AHN in neurologically healthy adult human subjects. For the data presented in Figs. 1 and 2, we used human samples obtained under tightly controlled conditions (Extended Data Fig. 1) and state-of-the-art methods for sample processing and preservation, to determine the most suitable conditions in which to study AHN in humans (Extended Data Figs. 2–5). These conditions allowed us to analyze the presence of DCX^+ immature neurons in the DG of 13 neurologically healthy subjects (aged between 43 and 87 years; Extended Data Fig. 1). We validated these results using four anti-DCX antibodies raised against different regions of the protein (Extended Data Fig. 4 and Supplementary Table 1). Moreover, DCX signal was analyzed in non-neurogenic brain regions (Fig. 1 and Extended Data Fig. 6). Next, we questioned whether cell subpopulations of immature neurons would exhibit a variable degree of maturation in the human DG (Fig. 2). We analyzed the expression of validated cell markers characteristic of different maturational stages during AHN in DCX^+ immature neurons. Finally, we analyzed the morphological characteristics of double-labeled cells. These analyses allowed us to outline the first model of the differentiation stages of human AHN (Fig. 2j).

Given that recent studies failed to detect immature neurons in the adult human hippocampus[9,10], we tested the influence of several parameters, such as fixation time and conditions (Extended Data Fig. 2) and diverse histological pretreatments of the tissue (Extended Data Figs. 3–5), on the detection of these cells. We determined that fixation time and conditions markedly influence the detection of markers of AHN in the human DG.

Study of AHN in patients with Alzheimer's disease. For the data presented in Figs. 3 and 4, AHN was examined in a group of 45 patients with AD between 52 and 97 years of age (distributed among the six Braak stages of the pathology[1,20]) (Extended Data Figs. 7 and 8) and then compared with that in 13 neurologically healthy (Braak stage 0) subjects. The total number (Fig. 3) and maturation (Fig. 4) of immature cells were determined.

Human subjects. A total of 58 subjects were included in the present study. Extended Data Figures 1 and 7 include detailed epidemiological data for these subjects. The use of brain tissue samples was coordinated by the local brain bank (Banco de Tejidos CIEN, Madrid, Spain), following national laws and international ethical and technical guidelines on the use of human samples for biomedical research purposes[27]. Samples were collected at the Banco de Tejidos CIEN (Madrid, Spain), the Hospital Clínico Universitario Virgen de la Arrixaca (Murcia, Spain), the Biobanco del Hospital Universitario Reina Sofia (Córdoba, Spain), and the Instituto Anatómico Forense (Madrid, Spain).

In all cases, brain tissue donation, processing, and use for research were in compliance with published protocols[28], which include obtaining informed consent for brain tissue donation from living donors and the approval of the whole donation process by the Ethical Committee of the Banco de Tejidos CIEN (committee approval reference 15-20130110).

The mean/median age of these groups of subjects is shown in Extended Data Fig. 7b. Statistically significant differences were found only between the age of controls and patients with Braak stage VI AD (Dunn's multiple-comparison test ($P=0.045$) for Kruskal–Wallis test).

Tau phosphorylation (AT100 epitope) in the anterior hippocampus, in the prefrontal, parietal, and temporal associative isocortex, and in the primary visual cortex was quantified at the neuropathology unit of the Banco de Tejidos CIEN to determine Braak stage, following previously described protocols[20,29]. All the neurologically healthy individuals included in this work were at Braak stage 0[29].

Hippocampal dissection and tissue fixation. Immediately after brain extraction, midsagittal sectioning was performed to separate the right and left hemispheres of the brain. All hippocampal samples included in this work were obtained from the right hemisphere. In fixation experiments (see below), the whole hippocampus was rapidly dissected on ice. For other experiments, a 0.5- to 1-cm-thick fragment that corresponded to the posterior portion of the anterior hippocampus was obtained. To this end, the posterior poles of both the mammillary bodies (level 32 in the Human Brain Atlas[26]) and the uncus (level 39 in the Human Brain Atlas[26]) were first identified. Next, a coronal 1-cm-thick slice of the whole hemisphere was obtained at this anatomical level. Anatomical references external to the hippocampus were established to select the sampling region. This is of particular importance to avoid any putative anatomical bias caused by hippocampal atrophy in patients with AD and to ensure that the sampling region was located at the same anatomical level for all subjects. After identification of the aforementioned anatomical references, a 0.5- to 1-cm-thick hippocampal sample corresponding to the posterior portion of the anterior hippocampus was rapidly dissected on ice and immediately immersed in freshly prepared 4% paraformaldehyde (PFA) (pH 7.4).

PMD ranged from 2.5 to 10 h for most of the samples, and only three samples with PMD of 16, 23, and 38 h were included in the study. A fixative solution of 4% PFA (pH 7.4) was freshly prepared immediately before autopsy by diluting a commercially available 16% PFA solution (Electron Microscopy Sciences, RT 15710) in 0.2 N phosphate buffer (PB) and distilled water (2:1:1). With the exception of fixation experiments, fixation time was strictly limited to 24 h. After being rinsed in PB, samples were immediately sectioned on a sliding-blade vibratome. Special attention was given to guaranteeing the highest homogeneity in tissue processing among samples. All autopsies were performed by the same pathologist, and tissue sectioning was performed by the same researcher.

Fixation experiments. To examine the influence of fixation time on the detection of markers of AHN in human brain tissue, the whole right hippocampus of four control subjects (Extended Data Fig. 1) was dissected on ice and divided into six 0.5-cm-thick blocks along the rostro–caudal axis of this structure. Each of these blocks was rapidly immersed in 4% PFA (pH 7.4) and was randomly assigned to one of the following fixation conditions: 1, 2, 6, 12, 24, or 48 h. After that time, blocks were rinsed thoroughly in 0.1 N PB and immediately sectioned on a sliding-blade vibratome (Extended Data Fig. 2).

To test the influence of fixatives on the detection of markers of AHN in human brain tissue, two 0.5-cm-thick blocks of the hippocampus from two control subjects (Extended Data Fig. 1) were fixed either in 4% PFA for 24 h at 4 °C or in 3.7% formalin for 6 months at 4 °C (Extended Data Fig. 2).

Tissue sectioning. To increase tissue robustness and prevent tissue damage when sectioning, hippocampal blocks were included in a 10% sucrose–4% agarose solution. Blocks were cut on a Leica VT-1200S sliding-blade vibratome (speed, 1–1.3; amplitude, 1.9), obtaining 50-µm sections. When necessary, sectioning speed and blade vibration were reduced (speed, 0.4; amplitude, 1.35) in samples fixed for a short time because of the low robustness of these samples. After vibratome sectioning, brain sections were immediately stored at −20 °C in a cryopreservative solution (30% polyethylene glycol, 10% 0.2 N PB, 30% glycerol, and 30% bidistilled water). All the above-mentioned histological procedures were completed less than 48 h after exitus (except for the sample with 38-h PMD).

Immunohistochemistry. Slices were rinsed in 0.1 N PB for 30 min at room temperature (three 10-min rinses under gentle shaking). To remove autofluorescence caused by aldehyde fixation, samples were incubated in a 0.5% sodium borohydride ($NaBH_4$; Sigma-Aldrich, 213462) solution. Next, a heat-mediated citrate buffer antigen retrieval (HC-AR) step was performed. Samples were rinsed five times in 0.1 N PB after completion of HC-AR. Dual or triple immunohistochemistry was then performed as described previously[18]. Incubation with primary antibodies was performed under gentle shaking at 4 °C for 5 d. Supplementary Table 1 and the Nature Research Reporting Summary document the primary antibodies used. To detect binding of primary antibodies, the Alexa Fluor–coupled fluorescent secondary antibodies indicated in Supplementary Table 1 were used. Incubation with secondary antibodies was performed under gentle shaking at 4 °C for 24 h. Either primary or secondary antibody was omitted in negative-control sections. All sections were counterstained for 10 min with DAPI (Merck; 1:5,000 dilution) to label nuclei. Immunohistochemistry was followed by a final autofluorescence elimination step. To this end, Autofluorescence Eliminator reagent (EMD Millipore, 2160) was used, following the manufacturer's instructions[30].Sections were mounted on gelatin-coated glass slides. A noncommercial antifade mounting medium (33% glycerol and 7.5% Mowiol, prepared in 0.2 M Tris-HCl, pH 8.5) was used to embed the sections. Slides were stored at room temperature and protected from light in opaque microscope slide cages. To prevent the decay of fluorescent signal intensity and to ensure homogeneity in the time elapsed for all subjects, confocal images were acquired within 1 month of section mounting.

Sodium borohydride, heat-mediated citrate buffer antigen retrieval, glycine, and Autofluorescence Eliminator reagent incubation procedures. Because of the decay of signal specificity and intensity and the increase in background observed with fixation times over 12 h (Extended Data Fig. 2), aldehyde, autofluorescence, and background elimination were necessary for most of the antibodies used (the need for performing this step is indicated in Extended Data Fig. 5, and Supplementary Table 1). Representative images of the results obtained with and without these steps are shown in Extended Data Figs. 2–5. We performed a complete series of combinations between the aldehyde elimination and antigen retrieval protocols to determine the most suitable histological procedures for studying AHN in human hippocampus. These combinations are summarized in Extended Data Fig. 3. Briefly, we assayed a range of concentrations of $NaBH_4$ (0%, 0.25%, 0.5%, 1%, 2%, and 5%, diluted in distilled water) alone or in combination with HC-AR protocols[31] and/or incubation with glycine.

For $NaBH_4$ incubation, brain sections were immersed in 1 ml of $NaBH_4$ solution for 30 min at room temperature and under gentle shaking. To this end,

24-well plastic plates were used and one or two sections belonging to the same patient were placed inside each well.

HC-AR was performed in 10-ml glass scintillation vials. To this end, individual sections or a series of 2–4 sections belonging to the same patient were immersed in 5 ml of a preheated 1× citrate buffer (pH 6.0) antigen retrieval solution (Vector, H-3300) (10× antigen retrieval stock solution was diluted in distilled water). Vials were exposed to 5–6 brief (10- to 20-s) cycles of microwave heating. Boiling of the liquid was avoided to prevent tissue damage. Next, vials were tightly closed and immersed in an 80 °C water bath for 20 min. Afterward, closed vials were left at room temperature for an additional 20 min.

For setup purposes, we tested the effect of an additional 30-min incubation with 1.5% glycine (room temperature, under gentle shaking). However, no further signal enhancement was observed after this step. Consequently, glycine incubation was not included in the subsequent experiments, given that five additional washes were required and this procedure caused unnecessary additional damage to the tissue.

After tissue pretreatment with the aforementioned protocols, sections were rinsed five times in 0.1 N PB and immunohistochemistry was performed as described above.

Moreover, to increase image cleanness, we used a final incubation step with Autofluorescence Eliminator reagent (Merck Millipore, 2160), which contains a solution of Sudan Black diluted in ethanol[32,33]. To this end, sections were immersed in 1 ml of 70% ethanol solution for 5 min under gentle shaking (24-well plastic plates were used). Next, sections were incubated in undiluted Autofluorescence Eliminator reagent for 5 min under vigorous shaking to prevent reagent precipitation. Finally, sections were washed three times in 70% ethanol (1-min washes under vigorous shaking), followed by three washes in 0.1 N PB and mounting.

Assessment of the specificity of DCX signal in human samples and preadsorption of anti-DCX antibodies with a synthetic DCX blocking peptide. To ensure the specificity of DCX staining in human tissue, we used four anti-DCX antibodies raised against different parts of the protein (Extended Data Fig. 4). The number of cells detected with each antibody and the percentage of co-labeled cells were determined. Moreover, we preadsorbed a polyclonal goat anti-DCX antibody (Santa Cruz) with a C-terminal synthetic peptide for human DCX (Abcam, ab19804). Preadsorption was performed by incubating equal amounts of the antibody and synthetic peptide overnight at 4 °C under shaking. Preadsorbed antibodies and those that were not preadsorbed were run separately in dot-blot experiments to ensure the absence of binding capacity, and immunohistochemistry was then performed as described above (Extended Data Fig. 4). The full-length unprocessed blot corresponding to Extended Data Fig. 4i is provided as source data.

Confocal microscopy. Confocal stacks of images were obtained with a LSM800 Zeiss confocal microscope, equipped with three GaAsP detectors. In fixation experiments, 10–20 stacks of images per subject and time point were obtained. In other experiments, 20 stacks per subject were used to stereologically estimate the density of DCX$^+$ cells. Stacks were obtained under a 40× oil-immersion objective (0.8 zoom; *xy* dimensions, 199.66 µm; *z* interval, 1 µm; pinhole dimensions, 0.9 Airy units). For colocalization analyses, a 63× oil-immersion objective (2.2 zoom; *xy* dimensions, 46 µm; *z* interval, 0.5 µm; pinhole dimensions, 0.9 Airy units) was used. For quantification of the total number of neurons in the GCL, a 63× oil-immersion objective (3.3 zoom; *xy* dimensions, 33.8 µm; *z* interval, 1.5 µm; pinhole dimensions, 1 Airy unit) was used. Images were randomly obtained from a minimum of ten sections per subject. To this end, the DG was first identified by means of a 10× dry objective in the DAPI channel. Next, stacks of images were obtained at randomly selected locations along the DG. Only the DAPI channel was visualized to select these locations. Moreover, researchers were blinded to subject diagnoses, both at the time of confocal image acquisition and when performing cell counts.

To further verify the specificity of DCX and PSA-NCAM staining, we performed cellular counts on three non-neurogenic regions, the EC and the CA1 and CA3 hippocampal subfields, for the 13 neurologically healthy subjects included in this work (Fig. 1 and Extended Data Figs. 1 and 6). Moreover, counts of NeuN$^+$ neurons were performed as a positive control (Fig. 1 and Extended Data Fig. 1). To this end, stacks of images were obtained under a 63× oil-immersion objective (*xy* dimensions, 101.401 µm; *z* interval, 1 µm; pinhole dimensions, 0.9 Airy units). To estimate cell densities in these regions, ten stacks per region and subject were obtained.

Stereological cell counts. Cell density was estimated stereologically using the physical dissector method adapted to confocal microscopy, as previously described[34]. Briefly, for determination of the density of DCX$^+$ cells in the DG, the GCL was traced on the DAPI channel of the *z* projection of each confocal stack of images, by using the freehand drawing tool in Fiji, and the area of this structure was calculated. This area was multiplied by the *z* thickness of the stack to calculate the reference volume. Next, DCX$^+$ cells inside the reference volume were counted on individual planes. This number was divided by the reference volume, and the density (number of cells/mm^3) of DCX$^+$ cells was calculated. A given cell was considered to be DCX$^+$ on the basis of clearly and unambiguously identifiable neuronal morphology. This definition included the presence of an elongated or oval-to-round cell nucleus and at least one neurite together with the absence of glial morphology, apoptotic characteristics in the DAPI channel, and autofluorescence in any of the other three channels. For each determination, DCX$^+$ cells were counted on 10–20 stacks of images obtained for at least 10 sections per subject. For colocalization analyses, at least 100 cells per subject and cell marker were analyzed. These data are represented as a percentage corresponding to the number of cells that were positive for the marker divided by the total number of DCX$^+$ cells. The density of NeuN$^+$ neurons in the DG and that of DCX$^+$, PSA-NCAM$^+$, and NeuN$^+$ cells in the EC and in the CA1 and CA3 hippocampal subregions were determined by counting the number of cells inside the reference volume (the whole dissector in this case) and dividing this number by the dissector volume, following a previously described methodology[18]. Researchers performing the experiments, imaging, and cell counting were blinded to the sex, age, PMD, and diagnoses of the subjects.

Morphometric determinations for DCX$^+$ cells. To determine the position of DCX$^+$ cells within the GCL, the hilar border of this structure, named the SGZ, was identified. The SGZ was defined as the one- to two-cell-thick portion of the GCL closer to the hilus. The number of cells located in the SGZ or within the GCL was counted; the percentage of cells located in each region is presented in graph form (Fig. 2o).

To determine the area of the soma (Fig. 2k–n), *z* stacks of images were obtained under a 63× oil-immersion objective, and the soma contour was drawn on the plane in which it was maximal and continuous around the nucleus. Next, the area was measured by using Fiji software. The DCX channel was used to measure soma area. Moreover, the number of primary neurites that emerged directly from the soma was counted (Fig. 2p). The percentage of cells in which 1, 2, 3, or 4 neurites were identified is shown in graph form. Finally, to identify the orientation of these neurites (perpendicular or parallel to the hilar border of the GCL), the angle between this border and the neurite was measured. A neurite was considered to have an orientation parallel to the SGZ (horizontal) in those cases in which the angle was ≤45°, whereas it was considered to be perpendicular in those cases in which angles ranged between 45° and 90° (vertical) (Fig. 2q).

Determination of the fluorescence intensity of phosphorylated tau (Ser396) and β-amyloid in the dentate gyrus. Single-plane three-channel (DAPI (blue), phosphorylated tau (green), and β-amyloid (red)) 16-bit images (40× oil-immersion objective (0.8 zoom; *xy* dimensions, 199.66 µm; pinhole dimensions, 0.9 Airy units)) were obtained with an LSM800 Zeiss confocal microscope. The location of these frames on the DG was randomly selected through observation of the DAPI channel. Acquisition settings (laser intensity, gain, and background subtraction) were kept constant for all images. Ten frames per subject were obtained. An invariant threshold was then set in Fiji for the phosphorylated tau or β-amyloid channel. The area above the threshold was measured in Fiji. Averaged values per subject are shown in Fig. 3b,c and Extended Data Fig. 8.

Statistical analysis. Statistical analyses were performed using GraphPad Prism 5 software. The D'Agostino and Pearson omnibus normality test was used to check the normality of sample distribution. For comparisons between two experimental groups, an unpaired two-sided Student's *t*-test was used in the case of normal sample distribution and a nonparametric test (Mann–Whitney *U* test) was used in cases in which normality could not be assumed. For comparisons between more than two experimental groups, data were analyzed by a one-way ANOVA test in the case of normal sample distribution or by a Kruskal–Wallis test in cases in which normality could not be assumed. When the one-way ANOVA and Kruskal–Wallis tests were statistically significant, Tukey and Dunn's multiple-comparison post hoc analyses, respectively, were used to compare the differences between individual groups. A two-sided Pearson's correlation test was applied to determine correlations between experimental variables. Graphs represent mean values ± s.e.m. A 95% confidence interval was used for statistical comparisons.

Reporting Summary. Further information on research design is available in the Nature Research Reporting Summary linked to this article.

Data availability

The data that support the findings of this study are available from the corresponding author upon reasonable request. All requests for raw and analyzed data will be promptly reviewed by the Center for Networked Biomedical Research on Neurodegenerative Diseases (CIBERNED) to determine whether the request is subject to any intellectual property or confidentiality obligations. Any materials that can be shared will be released via a material transfer agreement.

References

27. Martinez-Martin, P. & Avila, J. Alzheimer Center Reina Sofia Foundation: fighting the disease and providing overall solutions. *J. Alzheimers Dis.* **21**, 337–348 (2010).
28. International Society for Biological and Environmental Repositories. 2012 best practices for repositories collection, storage, retrieval, and distribution of biological materials for research. *Biopreserv. Biobank* **10**, 79–161 (2012).

29. Braak, H., Alafuzoff, I., Arzberger, T., Kretzschmar, H. & Del Tredici, K. Staging of Alzheimer disease–associated neurofibrillary pathology using paraffin sections and immunocytochemistry. *Acta Neuropathol.* **112**, 389–404 (2006).
30. Bolos, M. et al. Absence of CX3CR1 impairs the internalization of tau by microglia. *Mol. Neurodegener.* **12**, 59 (2017).
31. Llorens-Martin, M. et al. Tau isoform with three microtubule binding domains is a marker of new axons generated from the subgranular zone in the hippocampal dentate gyrus: implications for Alzheimer's disease. *J. Alzheimers Dis.* **29**, 921–930 (2012).
32. Llorens-Martin, M. et al. Peripherally triggered and GSK-3β-driven brain inflammation differentially skew adult hippocampal neurogenesis, behavioral pattern separation and microglial activation in response to ibuprofen. *Transl. Psychiatry* **4**, e463 (2014).
33. Diez-Fraile, A., Van Hecke, N., Guérin, C. J. & D'Herde, K. Applications of immunocytochemistry. *InTechOpen* **1**, 320 (2012).
34. Llorens-Martin, M., Torres-Aleman, I. & Trejo, J. L. Pronounced individual variation in the response to the stimulatory action of exercise on immature hippocampal neurons. *Hippocampus* **16**, 480–490 (2006).

a

SUBJECT	AGE	GENDER	PMD (hours)	DIAGNOSE	FIXATIVE
CONTROL 1	52	FEMALE	6	CANCER	4% PFA, 24 hours at 4 ºC
CONTROL 2	43	MALE	5	LEUKEMIA	4% PFA, 24 hours at 4 ºC (block 1), and 3.7% Formalin 6 months (block 2).
CONTROL 3	68	MALE	4	MULTISYSTEMIC ATROPHY	4% PFA, 24 hours at 4 ºC
CONTROL 4	78	MALE	3	AORTIC DISSSECTION	4% PFA, 24 hours at 4 ºC (block 1), and 3.7% Formalin 6 months (block 2).
CONTROL 5	75	FEMALE	5	CANCER	4% PFA, 24 hours at 4 ºC
CONTROL 6	85	MALE	23	PERITONITIS	4% PFA, 24 hours at 4 ºC
CONTROL 7	64	MALE	7	AORTIC DISSSECTION	4% PFA, 24 hours at 4 ºC
CONTROL 8	83	FEMALE	4	STROKE	4% PFA, 24 hours at 4 ºC
CONTROL 9	61	MALE	8	HEMORRAGIA	4% PFA, 24 hours at 4 ºC
CONTROL 10	61	FEMALE	8	CANCER	4% PFA, 1, 2, 6, 12, 24 and 48 hours at 4 ºC (!)
CONTROL 11	65	MALE	18	STROKE	4% PFA, 1, 2, 6, 12, 24 and 48 hours at 4 ºC (!)
CONTROL 12	63	MALE	38	STROKE	4% PFA, 1, 2, 6, 12, 24 and 48 hours at 4 ºC (!)
CONTROL 13	87	MALE	6.5	SEPSIS	4% PFA, 1, 2, 6, 12, 24 and 48 hours at 4 ºC (!)

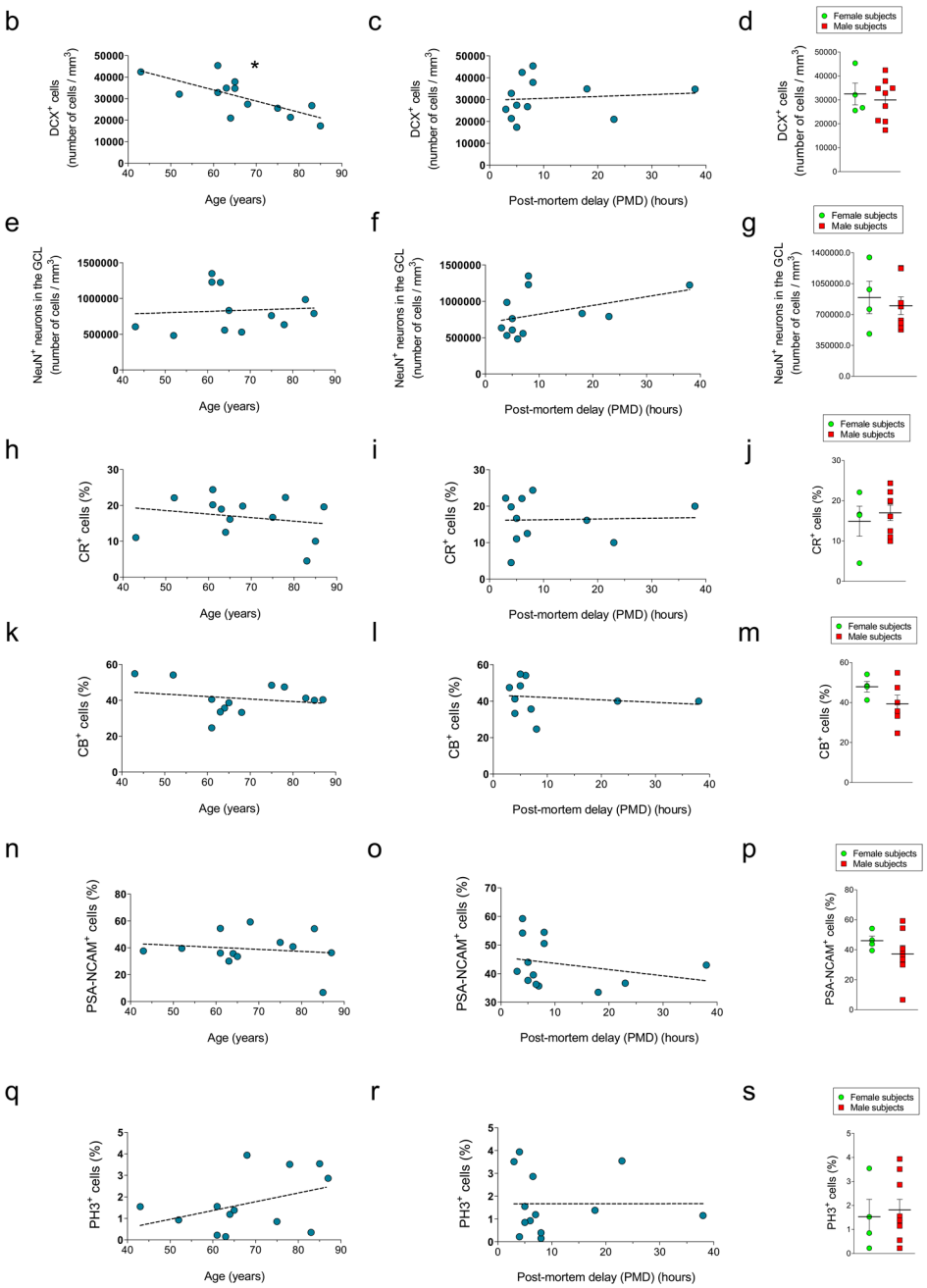

Extended Data Fig. 1 | See figure caption on next page.

Extended Data Fig. 1 | Control subjects included in this work. a, Epidemiological data for the 13 neurologically healthy control subjects included in this study. Age, sex, PMD, cause of death, type of fixative, and fixation conditions are indicated. A tissue block from each individual was fixed for 24 h in 4% PFA at 4 °C. Moreover, additional blocks of tissue from control 2 and control 4 were fixed in formalin for 6 months. Cases indicated with an exclamation mark were included in control fixation experiments, and additional blocks of tissue were therefore fixed for 1, 2, 6, 12, and 48 h in 4% PFA at 4 °C. **b**, Correlation between the age of subjects and the density of DCX^+ cells. There is a negative correlation between these parameters (two-sided Pearson's correlation, $r = -0.5842$, $P = 0.036$). **c**, Correlation between PMD and the density of DCX^+ cells (two-sided Pearson's correlation, $r = 0.1027$, $P = 0.7508$). **d**, Density of DCX^+ cells in male and female subjects (Mann–Whitney test, $U_{2,13} = 17.00$, $P = 0.9399$). The graph represents mean values ± s.e.m. **e**, Correlation between age of the subject and the density of $NeuN^+$ neurons in the GCL (two-sided Pearson's correlation, $r = 0.07694$, $P = 0.8122$). **f**, Correlation between PMD and the density of $NeuN^+$ neurons in the GCL (two-sided Pearson's correlation, $r = 0.4221$, $P = 0.1717$). **g**, Influence of sex on the density of $NeuN^+$ neurons in the GCL (Mann–Whitney test, $U_{2,13} = 14.00$, $P = 0.8081$). The graph represents mean values ± s.e.m. **h**, Correlation between age of the subject and the percentage of DCX^+ cells that are CR^+ (two-sided Pearson's correlation, $r = -0.3082$, $P = 0.3565$). **i**, Correlation between PMD and the percentage of DCX^+ cells that are CR^+ (two-sided Pearson's correlation, $r = 0.03674$, $P = 0.9146$). **j**, Influence of sex on the percentage of DCX^+ cells that are CR^+ (Mann–Whitney test, $U_{2,13} = 14.00$, $P = 0.8081$). The graph represents mean values ± s.e.m. **k**, Correlation between age of the subject and the percentage of DCX^+ cells that are CB^+ (two-sided Pearson's correlation, $r = -0.2768$, $P = 0.4710$). **l**, Correlation between PMD and the percentage of DCX^+ cells that are CB^+ (two-sided Pearson's correlation, $r = -0.1907$, $P = 0.6230$). **m**, Influence of sex on the percentage of DCX^+ cells that are CB^+ (Mann–Whitney test, $U_{2,13} = 5.00$, $P = 0.1714$). The graph represents mean values ± s.e.m. **n**, Correlation between age of the subject and the percentage of DCX^+ cells that are PSA-$NCAM^+$ (two-sided Pearson's correlation, $r = -0.1481$, $P = 0.6291$). **o**, Correlation between PMD and the percentage of DCX^+ cells that are PSA-$NCAM^+$ (two-sided Pearson's correlation, $r = -0.3241$, $P = 0.2526$). **p**, Influence of sex on the percentage of DCX^+ cells that are PSA-$NCAM^+$ (Mann–Whitney test, $U_{2,13} = 9.00$, $P = 0.2828$). The graph represents mean values ± s.e.m. **q**, Correlation between age of the subject and the percentage of DCX^+ cells that are $PH3^+$ (two-sided Pearson's correlation, $r = 0.4012$, $P = 0.1742$). **r**, Correlation between PMD and the percentage of DCX^+ cells that are $PH3^+$ (two-sided Pearson's correlation, $r = 0.00116$, $P = 0.9970$). **s**, Influence of sex on the percentage of DCX^+ cells that are $PH3^+$ (Mann–Whitney test, $U_{2,13} = 15.50$, $P = 0.7573$). The graph represents mean values ± s.e.m. In **b**–**s**, $n = 13$ control subjects. Twenty stacks of images were obtained for each subject. In colocalization analyses, at least 100 cells per subject were analyzed for each cell marker. *$0.05 > P \geq 0.01$ in two-sided Pearson's correlation.

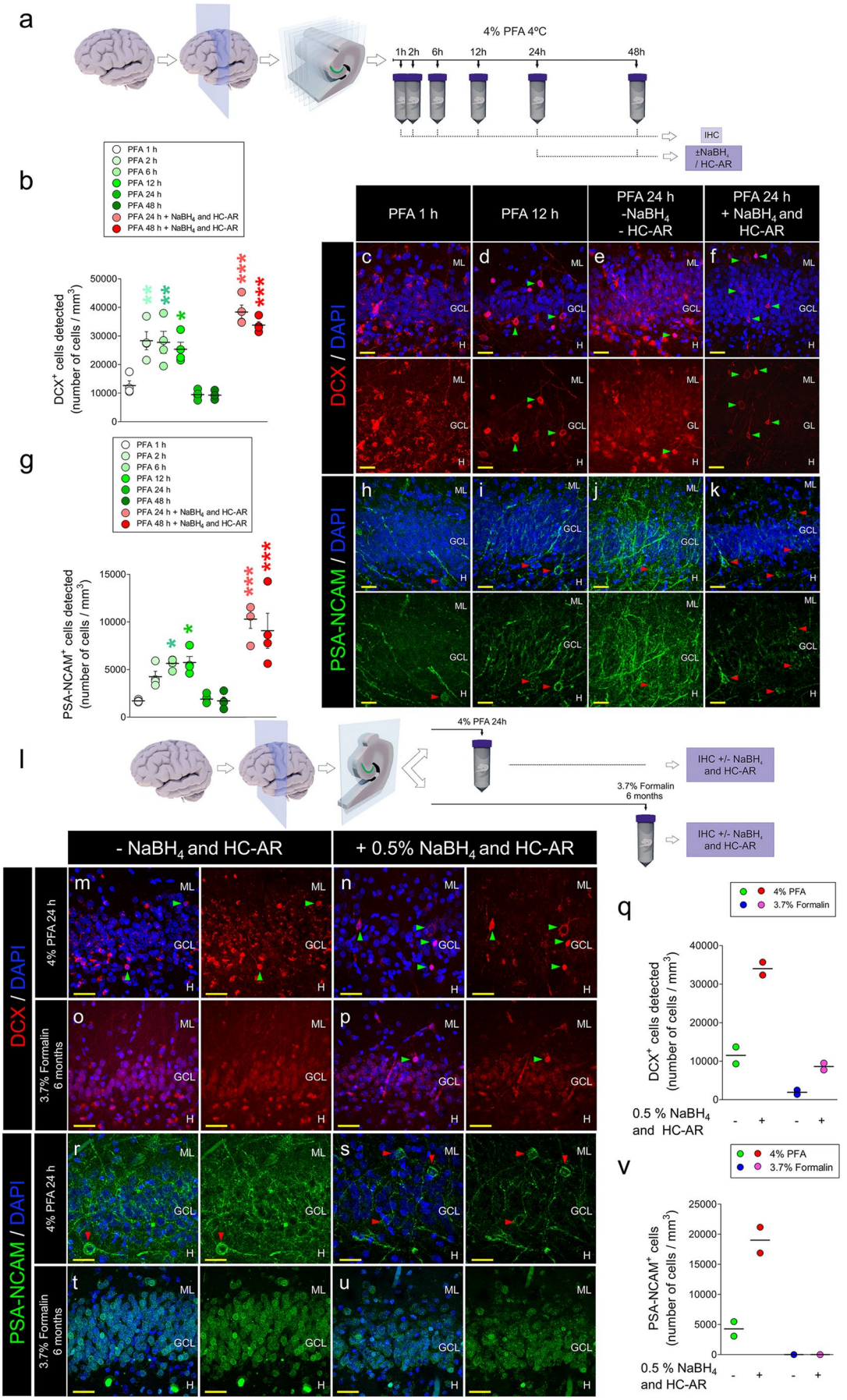

Extended Data Fig. 2 | See figure caption on next page.

Extended Data Fig. 2 | Influence of tissue fixation on the visualization of human adult hippocampal neurogenesis. a–k, Effects of fixation time. **a**, Schematic diagram of the experimental design. Briefly, a hippocampal fragment from four control subjects (61–87 years of age; Extended Data Fig. 1) was dissected and cut into 0.5-cm-thick blocks along the rostro–caudal axis of this structure. Each block was fixed for a different period of time in 4% PFA at 4 °C. **b–f**, Influence of fixation time on the visualization of DCX staining in the human DG. **b**, Number of DCX$^+$ cells detected after different fixation times (one-way ANOVA, $F_{8,32} = 23.90$, $P < 0.0001$). The graph represents mean values ± s.e.m. **c–f**, Representative images of DCX$^+$ cells, showing the differences in signal quality and background intensity caused by different fixation times. Weak tissue preservation, high-intensity background, and low intensity and specificity of the signal were observed after 1 h of fixation in 4% PFA. In contrast, 2–12 h of fixation in 4% PFA rendered a good signal/background ratio, although tissue robustness was minimal. In contrast, 24 and 48 h of fixation almost abolished DCX detection and substantially increased nonspecific background. Thus, given the marked decay in DCX signal after 12 h of fixation, samples fixed for 24 and 48 h were subjected to aldehyde elimination with 0.5% $NaBH_4$ and to a HC-AR protocol, which revealed the presence of thousands of DCX$^+$ cells in the adult human DG. Moreover, $NaBH_4$ and HC-AR allowed unambiguous identification of neuronal characteristics in these cells. **g–k**, Influence of fixation time on the visualization of PSA-NCAM staining in the human DG. **g**, Number of PSA-NCAM$^+$ cells detected (one-way ANOVA, $F_{8,32} = 16.54$, $P < 0.0001$). The graph represents mean values ± s.e.m. **h–k**, Representative images of PSA-NCAM staining in each fixation condition tested. Fixation times longer than 12 h impeded PSA-NCAM detection, and incubation with $NaBH_4$ + HC-AR was necessary to allow stereological estimation of the density of PSA-NCAM$^+$ cells. These histological pretreatments allowed identification of thousands of PSA-NCAM$^+$ cells in the DG. In **a–k**, $n = 4$ control subjects. 10–20 measurements were performed for each subject. **l–v**, Effects of formalin fixation on DCX and PSA-NCAM detection in the DG. **l**, Experimental design. Briefly, the hippocampi of two control subjects (control 2 and control 4; Extended Data Fig. 1) were dissected, and two 0.5-cm-thick blocks per subject were obtained. One of these blocks was fixed in 4% PFA for 24 h, whereas the other block was stored in 3.7% formalin for 6 months. **m–p**, Representative images of DCX staining in the different experimental conditions. **q**, Number of DCX$^+$ cells detected in samples fixed either in 4% PFA for 24 h or in 3.7% formalin for 6 months, with or without $NaBH_4$ + HC-AR pretreatment. The graph represents mean values. $NaBH_4$ + HC-AR steps increase the number of DCX$^+$ cells detected in samples fixed with both PFA and formalin. However, neither the intense background nor the marked decay in DCX signal caused by formalin fixation was counteracted by $NaBH_4$ + HC-AR. **r–u**, Representative images of PSA-NCAM staining in the different experimental conditions. **v**, Number of PSA-NCAM$^+$ cells detected in samples fixed either in 4% PFA for 24 h or in 3.7% formalin for 6 months, with or without $NaBH_4$ + HC-AR. The graph represents mean values. $NaBH_4$ + HC-AR increased the number of PSA-NCAM$^+$ cells detected in samples fixed with PFA. However, formalin fixation abolished the PSA-NCAM signal, and this effect was not prevented by $NaBH_4$ + HC-AR. In **l–v**, $n = 2$ control subjects. 10–20 measurements were performed for each subject. Yellow scale bars, 50 μm. Green triangles indicate DCX$^+$ cells; red triangles indicate PSA-NCAM$^+$ cells. In **b** and **g**, asterisks indicate significant differences with respect to the samples fixed for 1 h in Tukey post hoc comparisons. *$0.05 > P \geq 0.01$; **$0.01 > P \geq 0.001$; ***$P < 0.001$.

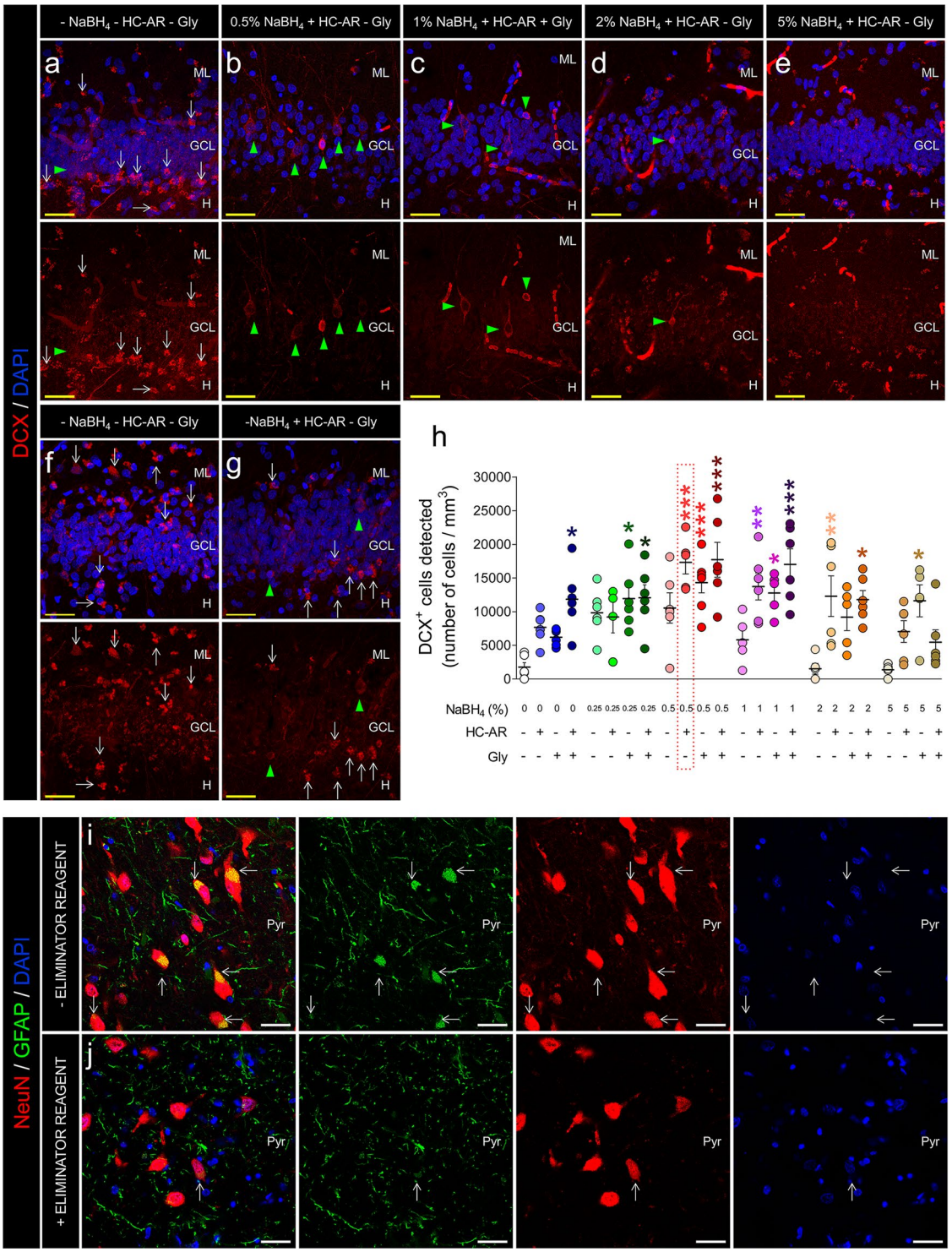

Extended Data Fig. 3 | See figure caption on next page.

Extended Data Fig. 3 | Identification of the most suitable histological procedures to study adult hippocampal neurogenesis in humans. To identify the most efficient sample pretreatment for eliminating background and autofluorescence caused by aldehyde fixation, we combined a range of concentrations of $NaBH_4$ with HC-AR and 1.5% glycine (Gly) incubation protocols. **a**–**h**, Representative images (**a**–**g**) and number (**h**) of DCX^+ cells detected in the different experimental conditions (one-way ANOVA, $F_{24,96} = 6.632$, $P < 0.0001$). The graph represents mean values ± s.e.m. Untreated sections (**a**) showed low signal specificity and intense nonspecific background, together with the presence of abundant autofluorescent aggregates (white arrows). These phenomena impeded the detection of DCX^+ cells. We assayed a range of $NaBH_4$ concentrations, alone or in combination with HC-AR and glycine incubation, and observed remarkable changes in signal specificity and background intensity. The best results were obtained after 30 min of incubation with 0.5% $NaBH_4$ together with HC-AR (**b**,**h**). These conditions rendered the highest specificity of the signal, allowed observation of the morphological characteristics of the cells, and provided significantly reduced background. Similarly good results were obtained when combining 0.5% and 1% $NaBH_4$ + HC-AR + glycine (**h**). However, glycine incubation was not used in subsequent experiments given that this step required an additional five washes, which increased the risk of tissue damage. In **c**–**e**, increasing the concentration of $NaBH_4$ over 2% caused an increase in background, thus preventing correct identification of DCX^+ cells. Application of HC-AR alone did not reduce the background or the intensity of autofluorescent aggregates, but it did allow better detection of DCX^+ cells, as a result of a subtle increase in signal intensity (**f**,**g**). **i**,**j**, Representative images of the CA1 hippocampal area showing the presence of intraneuronal autofluorescent aggregates in the green channel. The CA1 area was selected to show these aggregates because they are much more abundant in this area than in the DG. Incubation with Autofluorescence Eliminator reagent (Methods) after completion of immunohistochemistry caused a significant decrease in the signal for these aggregates, without affecting antibody detection. In **a**–**j**, $n = 6$ control subjects. Twenty measurements were performed for each subject. Yellow scale bars, 50 μm; white scale bars, 20 μm. Green triangles indicate DCX^+ cells; white arrows indicate nonspecific autofluorescent aggregates. $^*0.05 > P \geq 0.01$; $^{**}0.01 > P \geq 0.001$; $^{***}P < 0.001$. Asterisks indicate significant differences with respect to the samples that were not subjected to $NaBH_4$, HC-AR, or glycine pretreatment in Tukey post hoc comparisons.

a

CODE	ANTIGEN	COMPANY	HOST SPECIES	RRID/REFERENCE	IMMUNOGEN	CONCENTRATION	SIGNAL ENHANCEMENT
A	Doublecortin	SANTA CRUZ	GOAT (polyclonal)	RRID:AB_2088494	C-terminal (human DCX)	1:1,000	$NaBH_4$ +HC-AR (required)
B	Doublecortin	SANTA CRUZ	MOUSE (monoclonal)	RRID:AB_10610966	123-402 aa. (human DCX)	1:50	$NaBH_4$ +HC-AR (required)
C	Doublecortin	GLEESON LAB	RABBIT	-	16-mer polypeptide, C-terminal of human DCX (Cys-LPLSLDDSDSLGDSM)	1:200	$NaBH_4$ +HC-AR (required)
D	Doublecortin	ATLAS	RABBIT	RRID:AB_2674950	HSHCTEMQRLLPKLEMLTLG SSFCSLQGEFCQAMDSFTTV SHVGMCEETDASFNVFSPKF QFDRSHCQSLRFHQNMELDF GHFDERDKTSRNMR	1:50	$NaBH_4$ +HC-AR (required)

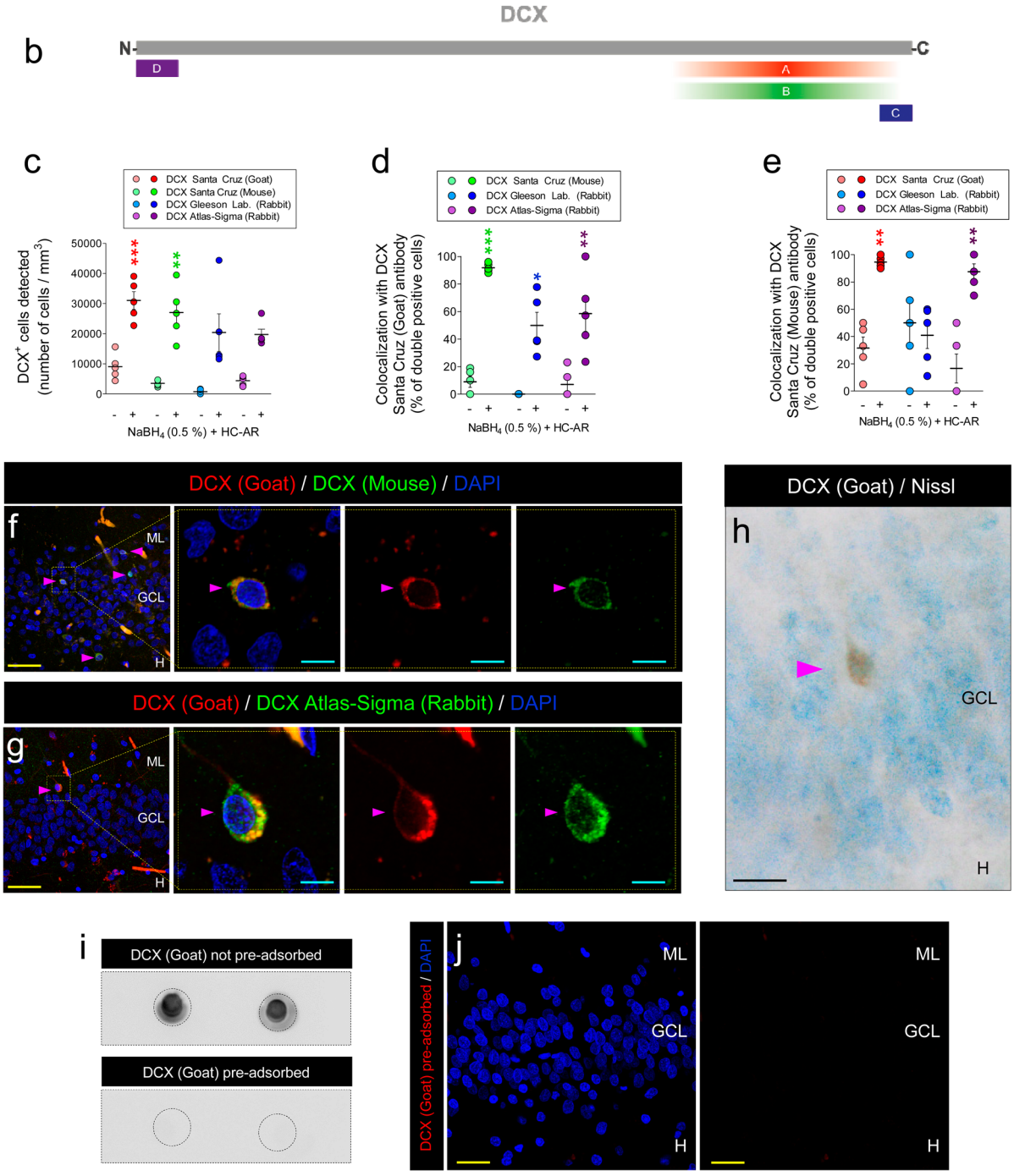

Extended Data Fig. 4 | See figure caption on next page.

Extended Data Fig. 4 | Validation of DCX$^+$ signal specificity. a, Four distinct anti-DCX antibodies were used. The company, host species, RRID, immunogen, concentration of use, and signal enhancement protocol applied are indicated. **b**, Schematic diagram of the DCX protein. The anti-DCX antibodies used were raised against different domains of the protein. **c**, Number of DCX$^+$ cells detected by using the distinct anti-DCX antibodies, with or without $NaBH_4$ and HC-AR sample pretreatment (one-way ANOVA, $F_{8,32}=15.07$, $P<0.0001$). The graph represents mean values ± s.e.m. $NaBH_4$ + HC-AR incubation was required to adequately detect DCX$^+$ cells for all the antibodies tested, although polyclonal goat anti-DCX (Santa Cruz) and mouse anti-DCX (Santa Cruz) antibodies gave the best results. **d**, Percentage of DCX$^+$ cells double labeled by a polyclonal goat anti-DCX antibody (Santa Cruz) and other anti-DCX antibodies (one-way ANOVA, $F_{6,24}=27.05$, $P<0.0001$). The graph represents mean values ± s.e.m. **e**, Percentage of DCX$^+$ cells double labeled by a monoclonal mouse anti-DCX antibody (Santa Cruz) and other antibodies (one-way ANOVA, $F_{6,24}=9.754$, $P<0.0001$). The graph represents mean values ± s.e.m. **f**,**g**, Representative images showing double labeling of DCX$^+$ cells by using a polyclonal goat anti-DCX antibody (Santa Cruz) and a monoclonal mouse anti-DCX antibody (Santa Cruz) (**f**) or a polyclonal goat anti-DCX antibody (Santa Cruz) and a polyclonal rabbit anti-DCX antibody (Atlas-Sigma) (**g**). On the basis of signal specificity, signal/background ratio, tissue penetration, and working concentration, we opted to use the polyclonal goat anti-DCX antibody (Santa Cruz) to perform all subsequent quantifications. **h**, Representative image of a DCX$^+$ cell counterstained with Nissl and visualized by immunohistochemistry. **i**, Dot-blot experiment showing no signal after preadsorption of polyclonal goat anti-DCX antibody (Santa Cruz) with a control synthetic DCX peptide that comprised the C-terminal domain of the protein. The full-length unprocessed blot is shown as source data. **j**, Representative image of DCX staining after sample incubation with preadsorbed polyclonal goat anti-DCX antibody (in red) showing no signal in the red channel. In **c**–**h**, $n=5$ control subjects. Twenty measurements were performed for each subject. In **i** and **j**, the experiment was repeated twice with identical results. Yellow scale bars, 50 μm; blue scale bars, 10 μm; black scale bars, 20 μm. Magenta triangles indicate DCX$^+$ cells. *$0.05>P\geq0.01$; **$0.01>P\geq0.001$; ***$P<0.001$. In **c**–**e**, asterisks indicate changes with respect to the samples that did not receive $NaBH_4$ + HC-AR treatment in Tukey post hoc comparisons. Source Data

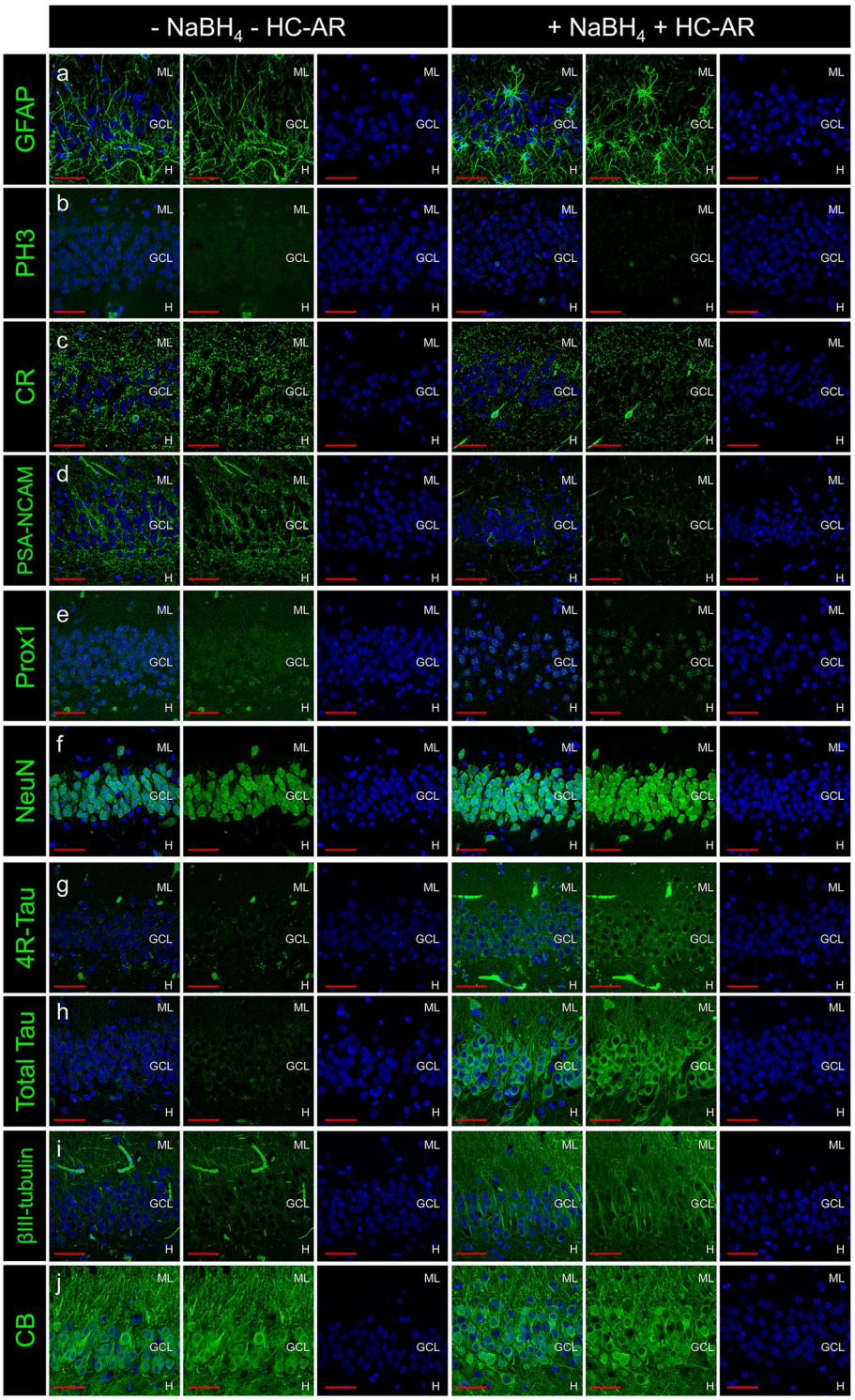

Extended Data Fig. 5 | Expression patterns of various cell markers in the human dentate gyrus. a–j, Representative images of the expression patterns of various cell markers in the DG, in samples with or without pretreatment with 0.5% $NaBH_4$ and HC-AR: GFAP (**a**), PH3 (**b**), CR (**c**), PSA-NCAM (**d**), Prox1 (**e**), NeuN (**f**), 4R-tau (**g**), total tau (**h**), βIII-tubulin (**i**), and CB (**j**). Red scale bars, 50 μm. $n = 13$ control subjects. Ten stacks of images were analyzed for each subject. Blue color indicates DAPI staining.

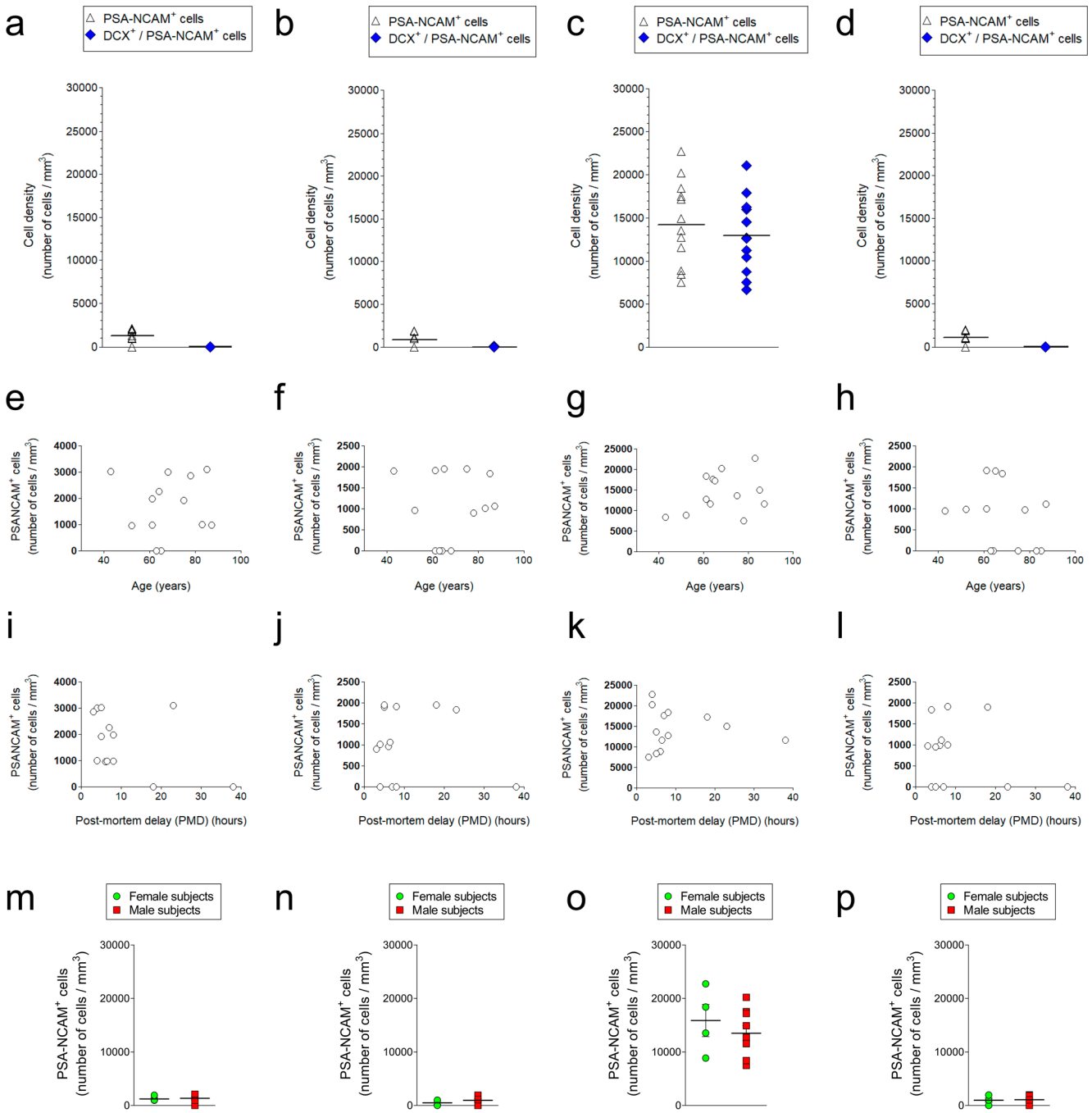

Extended Data Fig. 6 | Density of cells expressing PSA-NCAM and DCX in the entorhinal cortex and the hippocampus of neurologically healthy subjects. a, Density of PSA-NCAM$^+$ and PSA-NCAM$^+$DCX$^+$ cells in the EC. **b**, Density of PSA-NCAM$^+$ and PSA-NCAM$^+$DCX$^+$ cells in the CA1 hippocampal subfield. **c**, Density of PSA-NCAM$^+$ and PSA-NCAM$^+$DCX$^+$ cells in the DG. **d**, Density of PSA-NCAM$^+$ and PSA-NCAM$^+$DCX$^+$ cells in the CA3 hippocampal subfield. No PSA-NCAM$^+$DCX$^+$ cells were found in non-neurogenic regions. In **a**–**d**, $n=13$ control subjects. Graphs represent mean values. **e**, Correlation between age of the subject and the number of PSA-NCAM$^+$ cells in the EC (two-sided Pearson's correlation, $r=0.0346$, $P=0.911$). **f**, Correlation between age of the subject and the number of PSA-NCAM$^+$ cells in the CA1 hippocampal subfield (two-sided Pearson's correlation, $r=0.0444$, $P=0.885$). **g**, Correlation between age of the subject and the number of PSA-NCAM$^+$ cells in the DG (two-sided Pearson's correlation, $r=0.2965$, $P=0.325$). **h**, Correlation between age of the subject and the number of PSA-NCAM$^+$ cells in the CA3 hippocampal subfield (two-sided Pearson's correlation, $r=-0.299$, $P=0.321$). **i**, Correlation between PMD and the number of PSA-NCAM$^+$ cells in the EC (two-sided Pearson's correlation, $r=-0.0422$, $P=0.151$). **j**, Correlation between PMD and the number of PSA-NCAM$^+$ cells in the CA1 hippocampal subfield (two-sided Pearson's correlation, $r=-0.0916$, $P=0.766$). **k**, Correlation between PMD and the number of PSA-NCAM$^+$ cells in the DG (two-sided Pearson's correlation, $r=-0.0584$, $P=0.849$). **l**, Correlation between PMD and the number of PSA-NCAM$^+$ cells in the CA3 hippocampal subfield (two-sided Pearson's correlation, $r=-0.276$, $P=0.360$). In **e**–**l**, $n=13$ control subjects. **m**, Influence of sex on the number of PSA-NCAM$^+$ cells detected in the EC (Mann–Whitney test, $U_{2,13}=12.00$, $P=0.4140$). **n**, Influence of sex on the number of PSA-NCAM$^+$ cells detected in the CA1 hippocampal subfield (Mann–Whitney test, $U_{2,13}=13.00$, $P=0.4751$). **o**, Influence of sex on the number of PSA-NCAM$^+$ cells detected in the DG (Mann–Whitney test, $U_{2,13}=12.00$, $P=0.4140$). **p**, Influence of sex on the number of PSA-NCAM$^+$ cells detected in the CA3 hippocampal subfield (Mann–Whitney test, $U_{2,13}=17.50$, $P=1.000$). In **m**–**p**, $n=13$ control subjects. Graphs represent mean values ± s.e.m.

a

SUBJECT	AGE	GENDER	PMD (h)	BRAAK STAGE	CERAD	FIXATIVE
AD 1	52	MALE	6	I	0	4% PFA, 24 h at 4 °C
AD 2	67	FEMALE	10	I	0	4% PFA, 24 h at 4 °C
AD 3	82	MALE	5	I	0	4% PFA, 24 h at 4 °C
AD 4	73	MALE	9	I	0	4% PFA, 24 h at 4 °C
AD 5	60	MALE	5	I	0	4% PFA, 24 h at 4 °C
AD 6	76	MALE	3	II	0	4% PFA, 24 h at 4 °C
AD 7	73	MALE	6.5	II	0	4% PFA, 24 h at 4 °C
AD 8	73	MALE	10	II	0	4% PFA, 24 h at 4 °C
AD 9	83	FEMALE	5.5	III	3	4% PFA, 24 h at 4 °C
AD 10	70	FEMALE	9	III	2	4% PFA, 24 h at 4 °C
AD 11	93	FEMALE	16	III	0	4% PFA, 24 h at 4 °C
AD 12	80	FEMALE	5	III	0	4% PFA, 24 h at 4 °C
AD 13	87	FEMALE	3.5	IV	1	4% PFA, 24 h at 4 °C
AD 14	79	MALE	4.5	IV	2	4% PFA, 24 h at 4 °C
AD 15	62	MALE	5	IV	3	4% PFA, 24 h at 4 °C
AD 16	85	MALE	8.5	IV	2	4% PFA, 24 h at 4 °C
AD 17	93	FEMALE	5.5	V	3	4% PFA, 24 h at 4 °C
AD 18	92	MALE	4	V	3	4% PFA, 24 h at 4 °C
AD 19	73	MALE	5	V	3	4% PFA, 24 h at 4 °C
AD 20	80	MALE	5	V	3	4% PFA, 24 h at 4 °C
AD 21	84	MALE	4	V	3	4% PFA, 24 h at 4 °C
AD 22	85	MALE	2.5	V	3	4% PFA, 24 h at 4 °C
AD 23	93	MALE	8	V	3	4% PFA, 24 h at 4 °C
AD 24	86	FEMALE	5	V	3	4% PFA, 24 h at 4 °C
AD 25	78	FEMALE	6.5	V	3	4% PFA, 24 h at 4 °C
AD 26	89	FEMALE	4	V	3	4% PFA, 24 h at 4 °C
AD 27	90	MALE	5	V	3	4% PFA, 24 h at 4 °C
AD 28	81	MALE	10	V	3	4% PFA, 24 h at 4 °C
AD 29	87	FEMALE	5.5	V	3	4% PFA, 24 h at 4 °C
AD 30	91	FEMALE	3	VI	3	4% PFA, 24 h at 4 °C
AD 31	92	FEMALE	5-10	VI	3	4% PFA, 24 h at 4 °C
AD 32	83	FEMALE	3.5	VI	3	4% PFA, 24 h at 4 °C
AD 33	87	MALE	10	VI	3	4% PFA, 24 h at 4 °C
AD 34	90	FEMALE	10	VI	3	4% PFA, 24 h at 4 °C
AD 35	89	FEMALE	4.5	VI	3	4% PFA, 24 h at 4 °C
AD 36	60	MALE	4.5	VI	3	4% PFA, 24 h at 4 °C
AD 37	55	FEMALE	5	VI	3	4% PFA, 24 h at 4 °C
AD 38	92	MALE	6	VI	3	4% PFA, 24 h at 4 °C
AD 39	77	MALE	9	VI	3	4% PFA, 24 h at 4 °C
AD 40	97	FEMALE	6	VI	3	4% PFA, 24 h at 4 °C
AD 41	75	MALE	6	VI	3	4% PFA, 24 h at 4 °C
AD 42	90	FEMALE	5-7	VI	3	4% PFA, 24 h at 4 °C
AD 43	71	MALE	3.5	VI	3	4% PFA, 24 h at 4 °C
AD 44	81	MALE	6	VI	3	4% PFA, 24 h at 4 °C
AD 45	82	MALE	6	VI	3	4% PFA, 1, 2, 6, 12, 24 and 48 h at 4 °C (!)

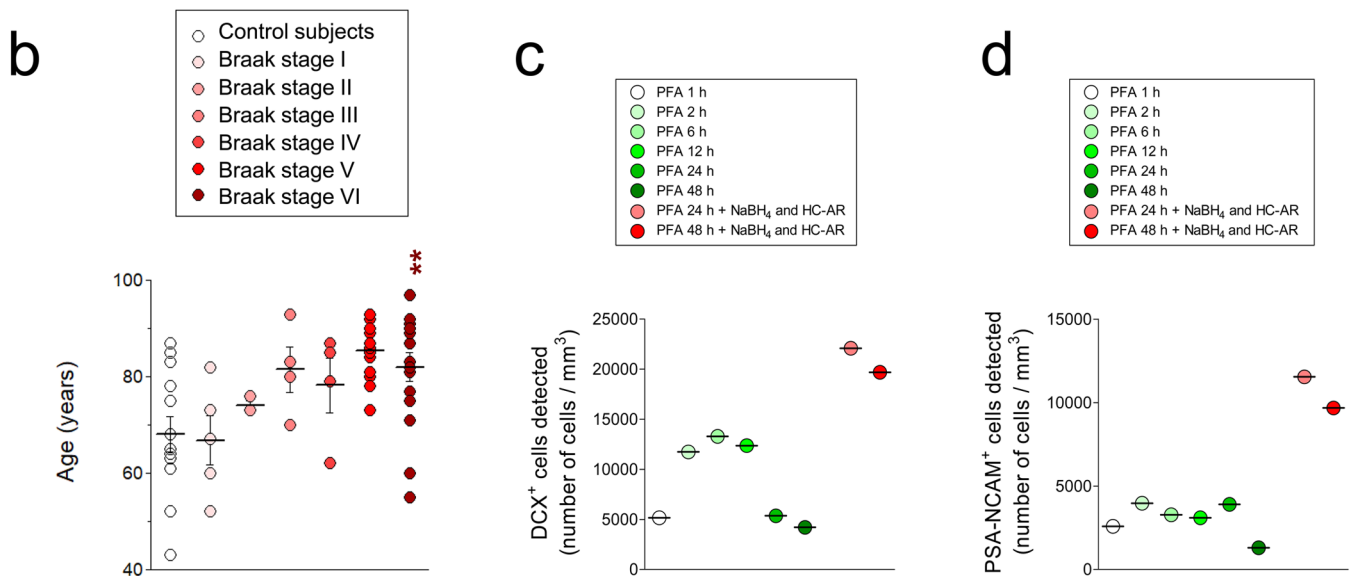

Extended Data Fig. 7 | See figure caption on next page.

Extended Data Fig. 7 | Patients with Alzheimer's disease included in this study. a, Epidemiological aspects of the patients with AD included in this study. Age, sex, PMD, Braak and CERAD stage, type of fixative, and fixation time are indicated. All samples were fixed for 24 h in 4% PFA at 4 °C. Moreover, the case indicated with an exclamation mark was included in control fixation experiments (**c**,**d**), and additional blocks were thus fixed for 1, 2, 6, 12, and 48 h in the same fixative at 4 °C. **b**, Age distribution in the groups of subjects (Kruskal–Wallis test, $K_{7,58} = 19.09$, $P = 0.0040$). The graph represents mean values ± s.e.m. $n = 13$ control subjects and 45 patients with AD. **c**, Density of DCX^+ cells detected in a fixation time experiment performed on samples from a patient with Braak stage VI AD (case AD 45; see **a**). **d**, Density of PSA-$NCAM^+$ cells detected in the same patient. In **c** and **d**, cell counts were performed independently on 20 sections from case AD 45 for each fixation time point. Graphs represent mean values. The same effects as those observed in control subjects take place, namely, a reduction in staining as fixation time increases and recovery of signal after $NaBH_4$ and HC-AR treatment. *$0.05 > P \geq 0.01$; **$0.01 > P \geq 0.001$; ***$P < 0.001$. In **b**, asterisks indicate significant differences with respect to control subjects in a Dunn's multiple-comparison test.

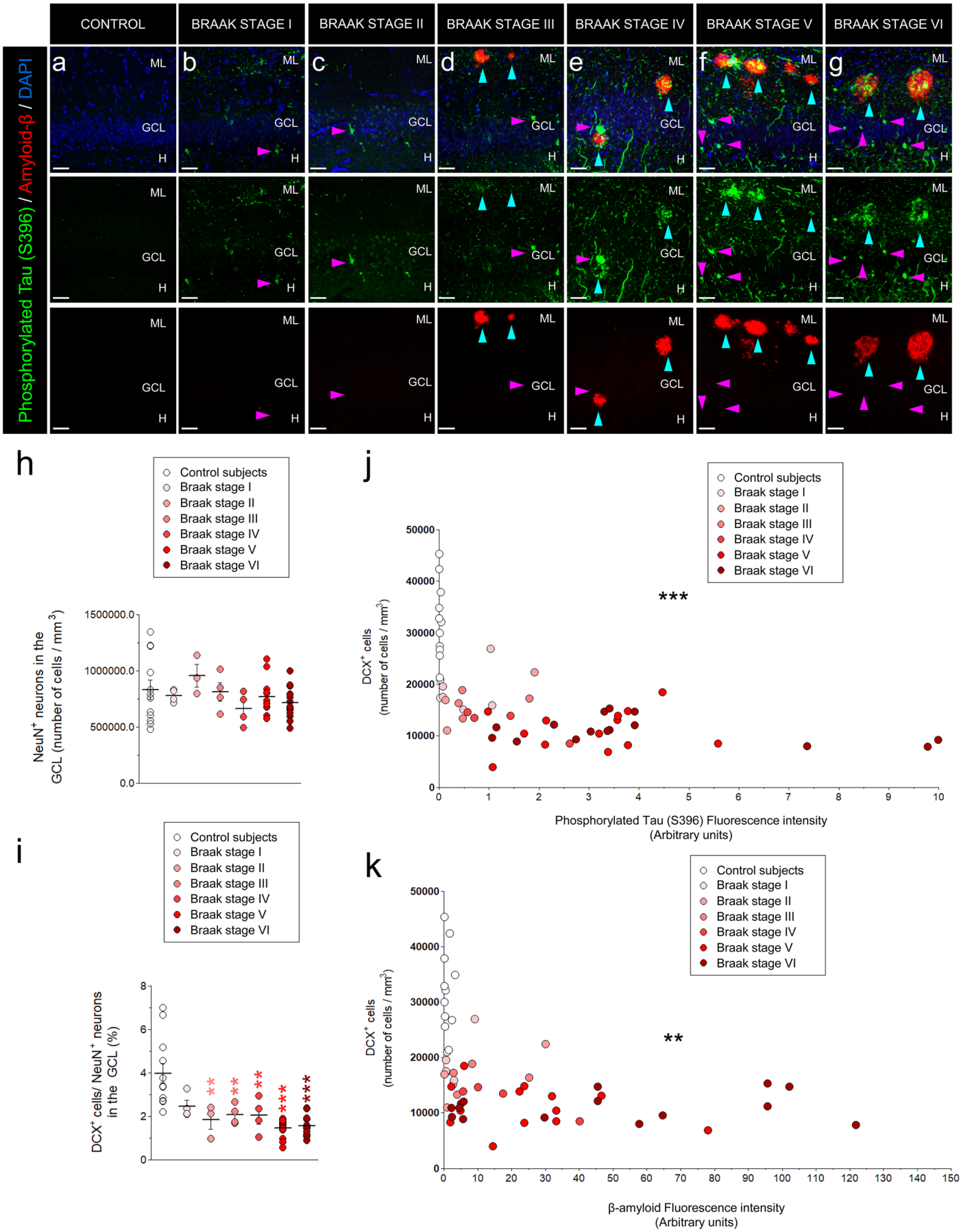

Extended Data Fig. 8 | See figure caption on next page.

Extended Data Fig. 8 | Histological alterations observed in the dentate gyrus of patients with Alzheimer's disease. a–**g**, Representative images of the DG of control subjects and patients with AD showing β-amyloid and phosphorylated tau (Ser396) staining in the DG along the six Braak stages of the disease[1,20]. The presence of these structures in the DG progressively increases as the disease advances. In **a**–**g**, $n = 13$ control subjects and 45 patients with AD. **h**, Density of NeuN$^+$ neurons in the GCL. No significant differences were observed during progression of the disease (one-way ANOVA test, $F_{7,58} = 1.135$, $P = 0.3565$). The graph represents mean values ± s.e.m. **i**, Ratio between the density of DCX$^+$ cells and the number of NeuN$^+$ neurons in the GCL (one-way ANOVA test, $F_{7,58} = 11.08$, $P < 0.0001$). The graph represents mean values ± s.e.m. **j**, Correlation between the number of DCX$^+$ cells and the fluorescence intensity of phosphorylated tau (Ser396) in the DG (Pearson's correlation, $r = -0.5316$, $P < 0.0001$). **k**, Correlation between the number of DCX$^+$ cells and the fluorescence intensity of β-amyloid in the DG (Pearson's correlation, $r = -0.3934$, $P = 0.0025$). In **h**–**k**, $n = 13$ control subjects and 45 patients with AD. Twenty measurements were performed for each subject to determine either the density of DCX$^+$ cells or the number of NeuN$^+$ neurons. Ten measurements were performed for each subject to determine the fluorescence intensity of phosphorylated tau (Ser396) and β-amyloid. $^{**}0.01 > P \geq 0.001$; $^{***}P < 0.001$. In **h** and **i**, asterisks indicate significant differences with respect to control subjects in Tukey post hoc comparisons. In **j** and **k**, asterisks represent statistical significance in Pearson's correlation. White scale bars, 50 μm. Blue triangles indicate β-amyloid senile plaques; magenta triangles indicate neurons that show tau phosphorylation, neurofibrillary tangles, or dystrophic neurites.

nature research

Corresponding author(s): Dr. Llorens-Martín, María

Reporting Summary

Nature Research wishes to improve the reproducibility of the work that we publish. This form provides structure for consistency and transparency in reporting. For further information on Nature Research policies, see Authors & Referees and the Editorial Policy Checklist.

Statistical parameters

When statistical analyses are reported, confirm that the following items are present in the relevant location (e.g. figure legend, table legend, main text, or Methods section).

n/a	Confirmed	
☐	☒	The exact sample size (*n*) for each experimental group/condition, given as a discrete number and unit of measurement
☐	☒	An indication of whether measurements were taken from distinct samples or whether the same sample was measured repeatedly
☐	☒	The statistical test(s) used AND whether they are one- or two-sided *Only common tests should be described solely by name; describe more complex techniques in the Methods section.*
☒	☐	A description of all covariates tested
☐	☒	A description of any assumptions or corrections, such as tests of normality and adjustment for multiple comparisons
☐	☒	A full description of the statistics including central tendency (e.g. means) or other basic estimates (e.g. regression coefficient) AND variation (e.g. standard deviation) or associated estimates of uncertainty (e.g. confidence intervals)
☐	☒	For null hypothesis testing, the test statistic (e.g. *F*, *t*, *r*) with confidence intervals, effect sizes, degrees of freedom and *P* value noted *Give P values as exact values whenever suitable.*
☒	☐	For Bayesian analysis, information on the choice of priors and Markov chain Monte Carlo settings
☐	☒	For hierarchical and complex designs, identification of the appropriate level for tests and full reporting of outcomes
☐	☒	Estimates of effect sizes (e.g. Cohen's *d*, Pearson's *r*), indicating how they were calculated
☐	☒	Clearly defined error bars *State explicitly what error bars represent (e.g. SD, SE, CI)*

Our web collection on statistics for biologists may be useful.

Software and code

Policy information about availability of computer code

Data collection	Fiji (ImageJ 64 bits 1.51s) was used to analyze confocal images
Data analysis	GraphPad Prism 5 was used to perform statistical tests

For manuscripts utilizing custom algorithms or software that are central to the research but not yet described in published literature, software must be made available to editors/reviewers upon request. We strongly encourage code deposition in a community repository (e.g. GitHub). See the Nature Research guidelines for submitting code & software for further information.

Data

Policy information about availability of data

All manuscripts must include a data availability statement. This statement should provide the following information, where applicable:

- Accession codes, unique identifiers, or web links for publicly available datasets
- A list of figures that have associated raw data
- A description of any restrictions on data availability

Data reported in this study are tabulated in the main text and Extended Data Figures and Tables. The data that support the findings of this study are available from the corresponding author (Dr. Llorens-Martín) upon request. All requests for raw and analyzed data will be promptly reviewed by the Center for Networked

Biomedical Research on neurodegenerative diseases (CIBERNED) to verify whether the request is subject to any intellectual property or confidentiality obligations. Any data and materials that can be shared will be released via a Material Transfer Agreement.

Field-specific reporting

Please select the best fit for your research. If you are not sure, read the appropriate sections before making your selection.

☒ Life sciences ☐ Behavioural & social sciences ☐ Ecological, evolutionary & environmental sciences

For a reference copy of the document with all sections, see nature.com/authors/policies/ReportingSummary-flat.pdf

Life sciences study design

All studies must disclose on these points even when the disclosure is negative.

Sample size	Sample size was not predicted. They were chosen based on previous literature. We have used a collection of human samples composed by 13 healthy control individuals and 45 Alzheimer´s disease patients. Pilot experiments provided an estimate of effect size, and indicated the appropriateness of sample sizes chosen.
Data exclusions	No data were excluded
Replication	Experimental findings were reproduced in at least three independent experiments. All replications were successful.
Randomization	Subjects were classified on the basis of neurological and neuropathological examination. Specifically, Braak-Tau stage was used for classification purposes.
Blinding	Investigators were blinded to group allocation when processing the tissue, performing cell counts or during confocal image acquisition.

Reporting for specific materials, systems and methods

Materials & experimental systems

n/a	Involved in the study
☒	☐ Unique biological materials
☐	☒ Antibodies
☒	☐ Eukaryotic cell lines
☒	☐ Palaeontology
☒	☐ Animals and other organisms
☐	☒ Human research participants

Methods

n/a	Involved in the study
☒	☐ ChIP-seq
☒	☐ Flow cytometry
☒	☐ MRI-based neuroimaging

Antibodies

Antibodies used	The following primary antibodies have been used in immunofluorescence: Goat anti-Doublecortin (DCX), Santa Cruz Biotechnology, RRID:AB_2088494, 1:1000; Mouse anti-Doublecortin (DCX), Santa Cruz Biotechnology, RRID:AB_10610966, 1:50; Rabbit anti-Doublecortin (DCX), kindly provided by Dr. Gleeson (University of California), 1:200; Rabbit anti-Doublecortin (DCX), Atlas Antibodies, RRID:AB_2674950, 1:50; Mouse anti-PSA-NCAM, Millipore, RRID:AB_9521, 1:1000; Rabbit anti-Calretinin, Swant, RRID:AB_261971, 1:500; Rabbit anti-Calbindin, Swant, RRID:AB_272122, 1:500; Rabbit anti-Phospho-Histone3, RRID:AB_310177, 1:500; Rabbit anti-Prox1, Reliatech, RRID:AB_10013821, 1:500; Rabbit anti-NeuN, Millipore, RRID:AB_10807945, 1:1000; Mouse anti-4R-Tau, Millipore, RRID:AB_310014, 1:500; Rabbit anti-total Tau, Synaptic Systems, RRID:AB_114719, 1:500; Mouse anti-BetaIII Tubulin, Promega, RRID:AB_430874, 1:1000; Mouse anti-GFAP, Millipore, RRID:AB_2294571, 1:1000; Rabbit anti-Phospho-Tau(S396), Thermo Fisher, RRID:AB_253374, 1:500; Mouse anti-Beta-Amyloid, Covance, RRID:AB_2564682, 1:1000. The following secondary antibodies were used to detect the binding of primary antibodies: Donkey Alexa-555 anti-goat, Thermo Fisher, A-21432, 1:1000; Donkey Alexa-488 anti-goat, Thermo Fisher, A-110552, 1:1000; Donkey Alexa-488 anti-rabbit, Thermo Fisher, A-21206, 1:1000; Donkey Alexa-647 anti-rabbit, Thermo Fisher, A-31573, 1:1000; Donkey Alexa-555 anti-rabbit, Thermo Fisher, A-31572, 1:1000; Donkey Alexa-488 anti-mouse, Thermo Fisher, A-21202, 1:1000; Donkey Alexa-647 anti-mouse, Thermo Fisher, A-31571, 1:1000; Donkey Alexa-555 anti-mouse, Thermo Fisher, A-31570, 1:1000.
Validation	- Goat anti-Doublecortin (DCX), Santa Cruz Biotechnology, RRID: AB_2088494: Validated by manufacturer to detect DCX of mouse, rat, human, and avian origin by WB, IP, IF, IHC, and ELISA. We further validated this antibody by pre-adsorption with a

specific blocking peptide (Abcam, Cat # ab19804). This validation was performed by dot blot and IHC.

- Mouse anti-Doublecortin (DCX), Santa Cruz Biotechnology, RRID:AB_10610966: Validated by manufacturer to detect DCX of mouse, rat, and human origin by WB, IP, IF, IHC, and ELISA.

- Rabbit anti-Doublecortin (DCX), kindly provided by Dr. Gleeson (University of California): Validated by Dr. Gleeson´s lab to detect DCX of mouse and human origin.

- Rabbit anti-Doublecortin (DCX), Atlas Antibodies, RRID:AB_2674950: Validated by manufacturer to detect DCX of human origin by IHC.

- Mouse anti-PSA-NCAM, Millipore, RRID:AB_9521: Validated by manufacturer to detect PSA-NCAM of human, rat, and mouse origin by ICC, IHC, RIA, and WB.

- Rabbit anti-Calretinin, Swant, RRID:AB_261971: Validated by manufacturer to detect Calretinin of human, monkey, rat, mouse, guinea pig, chicken, and fish origin by WB and IHC.

- Rabbit anti-Calbindin, Swant, RRID:AB_272122: Validated by manufacturer to detect Calbindin of human, monkey, rat, mouse, chicken, and fish origin by WB and IHC.

- Rabbit anti-Phospho-Histone3, RRID:AB_310177: Validated by manufacturer to detect phosphorylated histone 3 of mouse and human origin by ICC, IP, and WB.

- Rabbit anti-Prox1, Reliatech, RRID:AB_10013821: Validated by manufacturer to detect Prox1 of human origin by IF and WB.

- Rabbit anti-NeuN, Millipore, RRID:AB_10807945: Validated by manufacturer to detect NeuN of human, mouse, rat, and snail origin by ICC, IHC, IF, and WB.

- Mouse anti-4R-Tau, Millipore, RRID:AB_3100: Validated by manufacturer to detect 4R-Tau of human, rabbit, bovine, and mouse origin by IHC and WB.

- Rabbit anti-total Tau, Synaptic Systems, RRID:AB_114719: Validated by manufacturer to detect Tau of rat, mouse, and human origin by WB, IP, ICC, and IHC.

- Mouse anti-Beta-III-Tubulin, Promega, RRID:AB_430874: Validated by manufacturer to detect Beta-III-Tubulin of most mammalian species, specifically rat and human, by ICC, IHC, and WB.

- Mouse anti-GFAP, Millipore, RRID:AB_2294571: Validated by manufacturer to detect GFAP of chicken, human, porcine, and rat origin by IP, IHC, and WB.

- Rabbit anti-Phospho-Tau(S396), Thermo Fisher, RRID:AB_253374: Validated by manufacturer to detect phosphorylated Tau (S396) of human, mouse, and rat origin by WB, ICC, IF, and ELISA.

- Mouse anti-Beta-Amyloid, Covance, RRID:AB_2564682: Validated by manufacturer to detect Beta-Amyloid of human origin by WB, IHC, and direct ELISA.

Secondary antibodies were validated by manufacturer and have been extensively validated in the literature.

All the primary and secondary antibodies have been validated in our experiments by performing appropriate control tests in the absence of secondary and primary antibodies respectively.

Human research participants

Policy information about studies involving human research participants

Population characteristics	A total number of 58 subjects were included in the present study. Extended Data Figures 1 and 7 include detailed epidemiological data of these subjects, including gender and age. Statistically significant differences were found only between the age of Controls and Braak-Tau stage VI patients (Dunn´s Multiple comparison test (p = 0.045) for Kruskal-Wallis test). The population included 23 female and 35 male individuals. Tau phosphorylation (AT100 epitope) in the anterior hippocampus, prefrontal, parietal and temporal associative isocortex, and in the primary visual cortex was quantified at the neuropathology unit of the Banco de Tejidos CIEN to determine Braak-Tau stage, following previously described protocols. It should be noted that all the neurologically healthy individuals included in this work were at Braak-Tau 0 stage. Moreover, medical records were carefully examinated to determine the neurological status of the subjects. In all cases, brain tissue donation, processing, and use for research were in compliance with published protocols, which include the obtaining of informed consent for brain tissue donation from living donors, and the approval of the whole donation process by the local Ethical Committee.
Recruitment	Subjects were recruited on the basis of the brain tissue donation program coordinated by the neuropathology unit of the Banco de Tejidos CIEN. There are no potential self-selection bias that may be likely to impact results. Written informed consent was

obtained from all donnors, and the whole donation process was approved by the Ethical Committee of the Banco de Tejidos CIEN.